

AD _____

Award Number: DAMD17-03-1-0558

TITLE: Development and Characterization of Novel Volumetric Acquisition Orbits with an Application Specific Emission Tomograph for Improved Breast Cancer Detection

PRINCIPAL INVESTIGATOR: Caryl N. Brzymialkiewicz
Martin P. Tornai, Ph.D.

CONTRACTING ORGANIZATION: Duke University
Durham, NC 27708-0491

REPORT DATE: August 2005

TYPE OF REPORT: Annual Summary

PREPARED FOR: U.S. Army Medical Research and Materiel Command
Fort Detrick, Maryland 21702-5012

DISTRIBUTION STATEMENT: Approved for Public Release;
Distribution Unlimited

The views, opinions and/or findings contained in this report are those of the author(s) and should not be construed as an official Department of the Army position, policy or decision unless so designated by other documentation.

20060315 037

REPORT DOCUMENTATION PAGEForm Approved
OMB No. 0704-0188

Public reporting burden for this collection of information is estimated to average 1 hour per response, including the time for reviewing instructions, searching existing data sources, gathering and maintaining the data needed, and completing and reviewing this collection of information. Send comments regarding this burden estimate or any other aspect of this collection of information, including suggestions for reducing this burden to Department of Defense, Washington Headquarters Services, Directorate for Information Operations and Reports (0704-0188), 1215 Jefferson Davis Highway, Suite 1204, Arlington, VA 22202-4302. Respondents should be aware that notwithstanding any other provision of law, no person shall be subject to any penalty for failing to comply with a collection of information if it does not display a currently valid OMB control number. PLEASE DO NOT RETURN YOUR FORM TO THE ABOVE ADDRESS.

1. REPORT DATE (DD-MM-YYYY) 01-08-2005		2. REPORT TYPE Annual Summary		3. DATES COVERED (From - To) 07/14/04-07/13/05	
4. TITLE AND SUBTITLE Development and Characterization of Novel Volumetric Acquisition Orbits with an Application Specific Emission Tomograph for Improved Breast Cancer Detection				5a. CONTRACT NUMBER	
				5b. GRANT NUMBER DAMD17-03-1-0558	
				5c. PROGRAM ELEMENT NUMBER	
6. AUTHOR(S) Caryl N. Brzymialkiewicz Martin P. Tornai, Ph.D. E-Mail: cnb3@duke.edu				5d. PROJECT NUMBER	
				5e. TASK NUMBER	
				5f. WORK UNIT NUMBER	
7. PERFORMING ORGANIZATION NAME(S) AND ADDRESS(ES) Duke University Durham, NC 27708-0491				8. PERFORMING ORGANIZATION REPORT NUMBER	
9. SPONSORING / MONITORING AGENCY NAME(S) AND ADDRESS(ES) U.S. Army Medical Research and Materiel Command Fort Detrick, Maryland 21702-5012				10. SPONSOR/MONITOR'S ACRONYM(S)	
				11. SPONSOR/MONITOR'S REPORT NUMBER(S)	
12. DISTRIBUTION / AVAILABILITY STATEMENT Approved for Public Release; Distribution Unlimited					
13. SUPPLEMENTARY NOTES					
14. ABSTRACT Abstract on next page					
15. SUBJECT TERMS Nuclear Medicine Imaging, SPECT, Dedicated Tomographic Breast Imaging, Mammothomography					
16. SECURITY CLASSIFICATION OF:			17. LIMITATION OF ABSTRACT Unclassified	18. NUMBER OF PAGES 31	19a. NAME OF RESPONSIBLE PERSON USAMRMC
a. REPORT Unclassified	b. ABSTRACT Unclassified	c. THIS PAGE Unclassified			19b. TELEPHONE NUMBER (include area code) 301-619-7325

Abstract

The overall goal of this work is to develop, implement, and evaluate novel three-dimensional acquisition orbits used in conjunction with a dedicated emission mammotomography system, to be used as a potential secondary diagnostic tool. This novel nuclear medicine based molecular imaging technique utilizes camera trajectories that sample a pendant, uncompressed breast, which are evaluated with respect to various breast shapes and sizes. Phantom measurements have demonstrated that lesions near the chest wall can be visualized for both large and small sized breasts, and furthermore, that axillary imaging is possible even with minimal system tilt. The use of additional bed shielding, simulated here with a lead sheet, was also investigated. Preliminary results suggest the lead shield may hinder lesion detectability. Future work includes the addition of a patient bed, which is expected to further complicate positioning, and which may or may not include lead lining pending further studies.

Table of Contents

Cover.....	
SF 298.....	
Table of Contents.....	
Introduction.....	4
Body.....	4
Key Research Accomplishments.....	10
Reportable Outcomes.....	10
Conclusions.....	11
References.....	11
Appendices.....	13

Introduction

The overall goal of this work is to develop, implement, and evaluate novel three-dimensional acquisition orbits used in conjunction with a dedicated emission mammotomography system, which may allow for earlier detection of a primary breast cancer. The tomographic gantry central to the ASET allows for camera positioning anywhere about an uncompressed, pendant breast in inverted hemispherical volumes [1, 2]. The key benefits of imaging in this geometry include the increased separation of the breast tissue from the nearby body containing background and the ability to image an uncompressed breast. One main advantage of 3D orbits that utilize increased polar tilt is then an increased viewable breast volume, potentially into the chest wall region [1]. However, with increased tilt angle, the camera may directly view cardiac and hepatic regions, which could contribute primary background contamination to the 2D projection images of the breast. Scintimammography phantom imaging studies indicate that scatter from cardiac and hepatic background can significantly contaminate the primary lesion signal [3]. Studies with clinical SPECT gamma cameras using simple tilted-parallel-beam (TPB) vertical-axis-of-rotation (VAOR) orbits [4], and simulations of somewhat more sophisticated orbits [5] have shown the potential effectiveness of dedicated SPECT breast imaging approaches that use non-standard camera orientations. Lesion contrast and SNR improve by nearly a factor of three when using a clinical camera with tilted-parallel-beam as compared to low noise planar (2D) images [4]. However, current clinical SPECT scanners are not only limited by the ROR that they can achieve, but also, by the trajectories possible with the gantry. Through its combined fully computed controlled variable radius-of-rotation, polar and azimuthal angular positioning, the ASET has opened up a new class of volumetric orbits for tomographic acquisition not previously possible with clinical scanners.

Body

Task 2. Development and investigation of novel orbits. (Please see Appendix A for original statement of work).

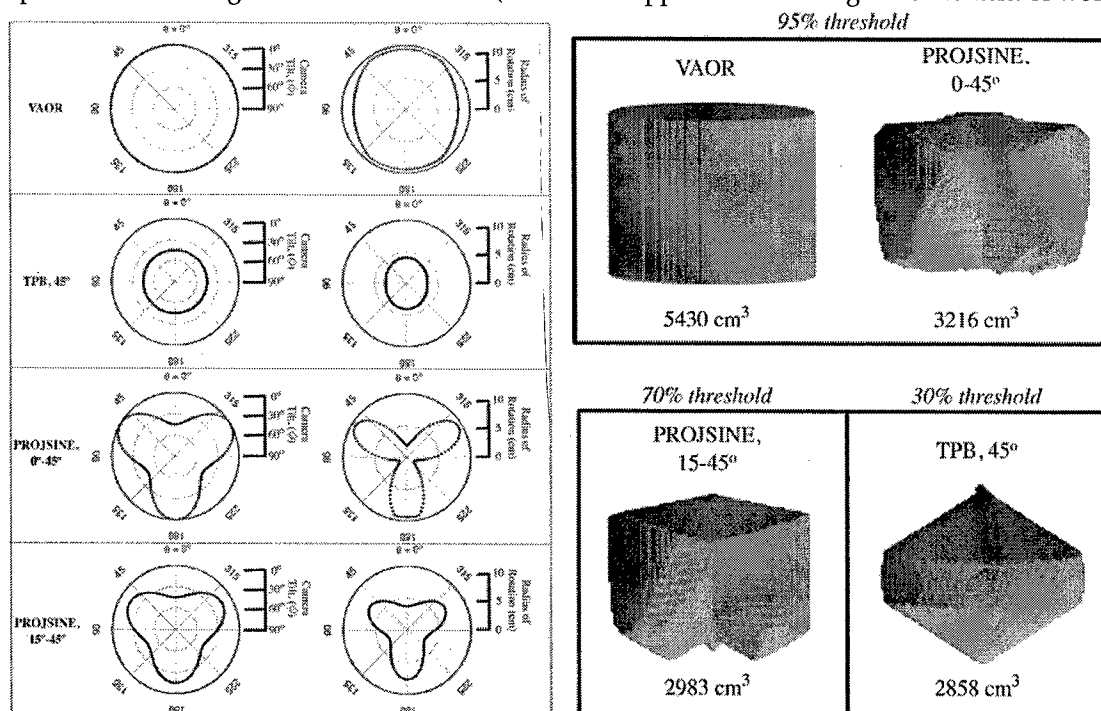


Fig. 1. (LEFT) Within each box, the left plot shows polar camera tilt as a function of the azimuthal angle for each examined orbit; the right plot shows the radius of rotation. (RIGHT) Voxelized Orlov Volumes of the orbits. VAOR and PROJSINE 0-45° are shown at the 95% threshold. Because TPB 45° and PROJSINE 15-45° do not meet Orlov's criteria and thus do not completely sample the breast, they are instead shown at their maximum threshold. The threshold is the percent solid angle that is sampled.

Volumetric acquisition orbits that more-nearly-completely sample the pendant, uncompressed breast were investigated, with respect to various breast shapes and sizes (as a continuation of Task 2(a)). Several orbits were implemented to compensate for the positioning demands that are required for different breast sizes (Fig. 1); while a general orbit design may remain the same between two different breasts, the absolute polar tilt range and ROR range may vary. Thus, these orbits were designed with a specific focus on orbit parameters of: viewable breast volume, radius-of-rotation, location of the center-of-rotation, and polar tilt angle, considering calculated Orlov Volumes [6].

Calculated Orlov Volumes are shown in Fig. 1. We evaluated this newer set of developed orbits with measurements of lesion contrasts and signal-to-noise ratios in anthropomorphic breast phantoms with and without additional torso backgrounds, and (2) examining the effect of various concentration ratios and various lesion sizes on image quality, to characterize the limitations of the system's performance. For detailed methods and results from the breast-only studies, and preliminary reconstructions of the bed shielding studies, please see Appendix B.

Detailed descriptions of the methods for the additional bed shielding experiments are given in Appendix B. Photographs of the setup are shown in Fig. 2. Newly reconstructed results of the bed shielding studies are shown in Fig. 3.

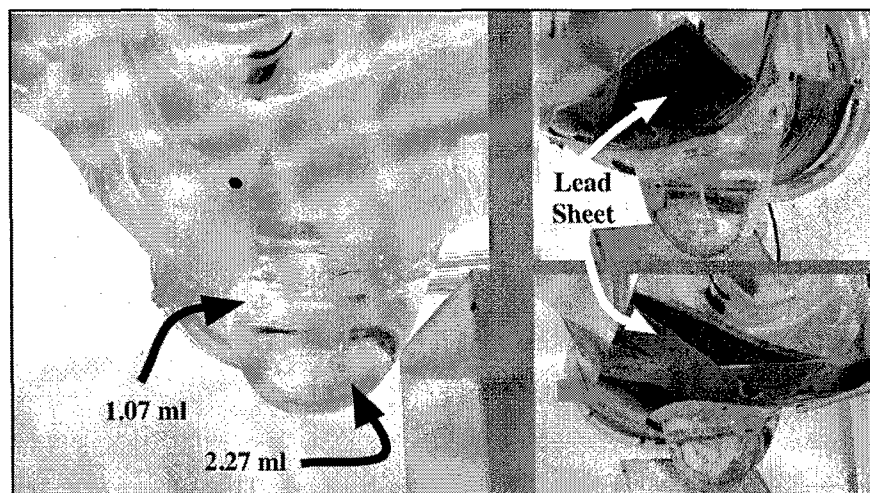


Fig. 2. Photographs of: (LEFT) 1060 ml breast phantom attached to the torso, with lesion sizes as labeled; (RIGHT) Two vantages of the lead sheet used to shield the 'patient'.

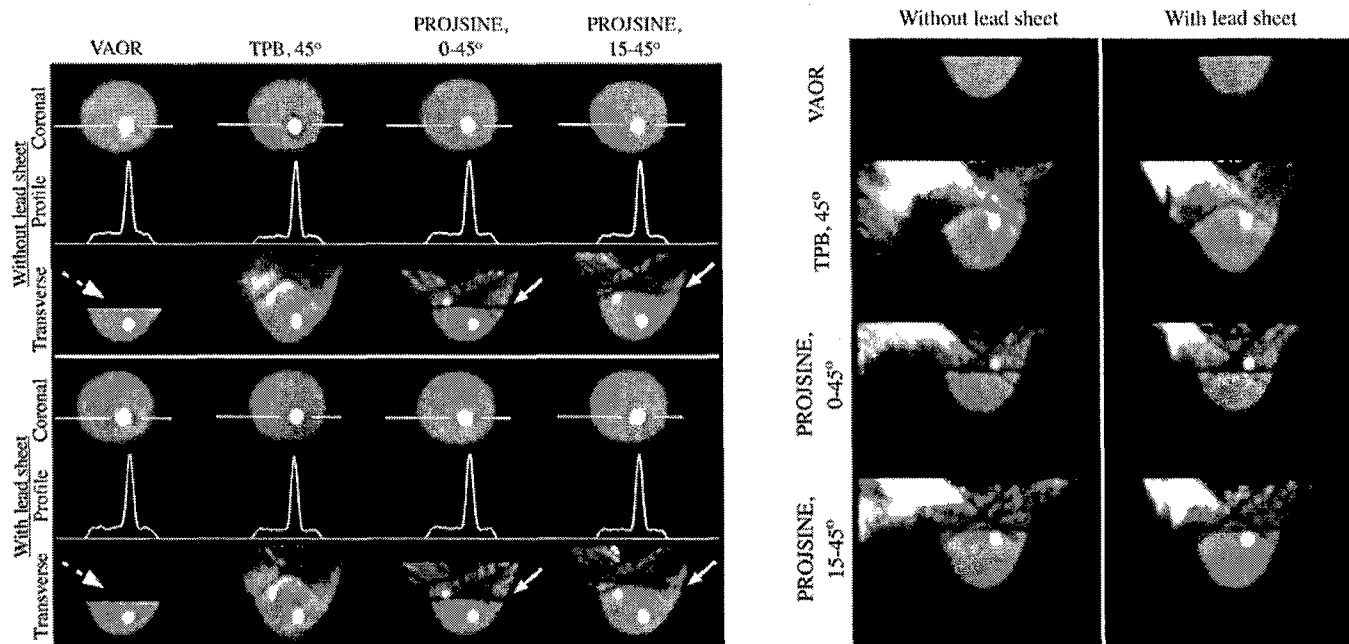


Fig. 3. Images from reconstructed 1060 ml breast + filled torso data (OSEM, 2.5 mm³ voxels, 2nd iteration, calculated attenuation correction, Hann filter applied) with and without the lead sheet. (LEFT) 3-pixel wide profiles drawn through the 2.27 ml lesion. The lesion near the chest wall is not visible with VAOR (dashed white arrow) and artifacts move further into the breast for the PROJSINE 15-45° case as compared to PROJSINE 0-45° (smaller white arrows). (RIGHT) More background activity is visible in the sagittal views without the lead sheet; increased tilt views the heart and liver more directly.

Employing 3D data acquisition camera trajectories with increased polar camera tilt, we have demonstrated that lesions near the chest wall can be visualized for both large and small sized breasts (Fig. 3 and Appendix B). As expected, the shapes of the reduced-artifact regions in the reconstructed images correspond to the respective shapes of the calculated Orlov Volumes (Fig. 1). Because previous studies have suggested the tomographic sampling criteria for completeness may not be as strict as initially anticipated, we relaxed the restrictions on the camera polar tilt. This allowed the COR to move further into the breast, which increased the reduced-artifact region of the breast (Fig. 3), thus allowing easier visualization of lesions near the chest wall. If a lesion is suspected near the chest wall, then to confirm diagnosis of a lesion in that region one may utilize more camera tilt and relax the sampling criteria (e.g., PROJSINE 15-45°); to determine whether a smaller lesion and/or lesion of low radiopharmaceutical uptake is present anywhere in the breast, an orbit such as TPB, with its decreased ROR, may be more appropriate.

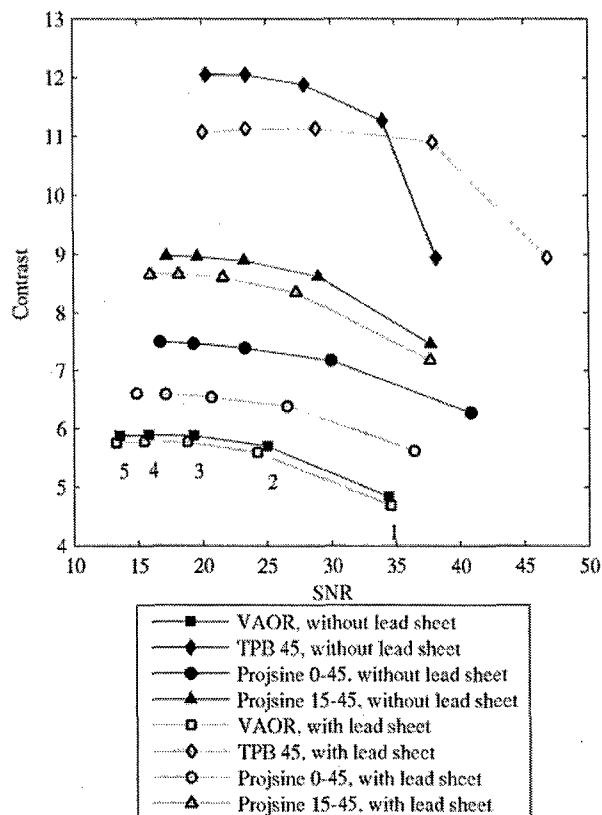


Fig. 4 Contrast versus SNR for the reconstructed breast + torso data and the 2.27 ml lesion. Iterations labeled next to VAOR. Patient shielding yields slightly lower SNR and contrast values.

Preliminary results suggest that the lead shield may actually hinder lesion detectability, as the SNRs and contrasts slightly decrease (Fig. 4). One possible cause of this decrease may be from scattered counts of photons that emerge from the breast and get deflected back to the detector by the shield. This trend may or may not be indicative of the true nature of the effect of the shield; with only one measurement of each case, the current measurements are likely within error bars of each other. Furthermore, these measurements do not account for the contralateral breast, which would also contribute to the background. The lead shield may not be necessary, given a judicious choice of the acquisition orbit and subsequent design parameters to minimize direct views of the heart and liver, and utilizing the superior energy resolution of the CZT camera to diminish the effect of secondary scattered background contamination. Because a lead shield may preclude close proximity positioning of the detector, however, this preliminary result will be further studied, with the phantoms positioned on a patient bed rather than freely suspended from a phantom holder.

In order to determine which acquisition and reconstruction parameters may be most optimal (Task 2(c)), software was developed to process previously acquired list-mode data. One goal of the post-processing was to examine the resulting normalized photopeak counts extracted from the summed energy spectra as a function of the azimuthal position (Fig. 5). The increased photopeak counts from $45 < \theta < 135$ (where θ is the azimuthal angle of the rotation stage) are due to contamination from the heart and liver, which provide both primary and secondary scattered counts. Increased polar tilt angles, which view the heart and liver more directly, are a direct cause of the increase in the number of photopeak counts. The larger polar tilt values correspond to the increases in photopeak counts (compare Figs. 1 and 5, TPB, 45°, PROJSINE 0-45° and PROJSINE 15-45°)

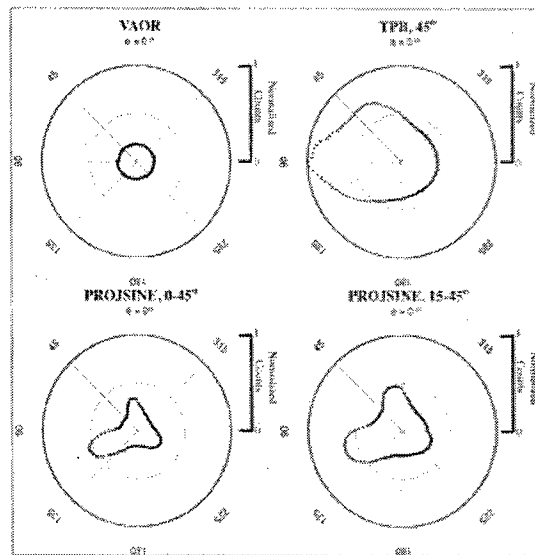


Fig. 5. Normalized photopeak counts as a function of the azimuthal position, which includes all valid events from the original list-mode data files within a $\pm 8\%$ energy window.

Additionally, we ran studies with simulated repeated measurements to determine the variability in SNR and contrast for each orbit given in Fig. 1, given various reconstruction and acquisition parameters. Initial reconstructions typically do not include calculated attenuation compensation nor additional post-processing with 3D filtering; subsequent re-reconstructions included these components, adding each independently (i.e., first add attenuation compensation in the routine, then apply 3D filtering). Results from the different reconstruction techniques are given in Fig. 6 and suggest that for orbits that employ increased polar tilt, contrasts are better without attenuation compensation, while SNRs remain about the same. In all cases, as expected, filtering increases the SNRs and decreases the contrasts.

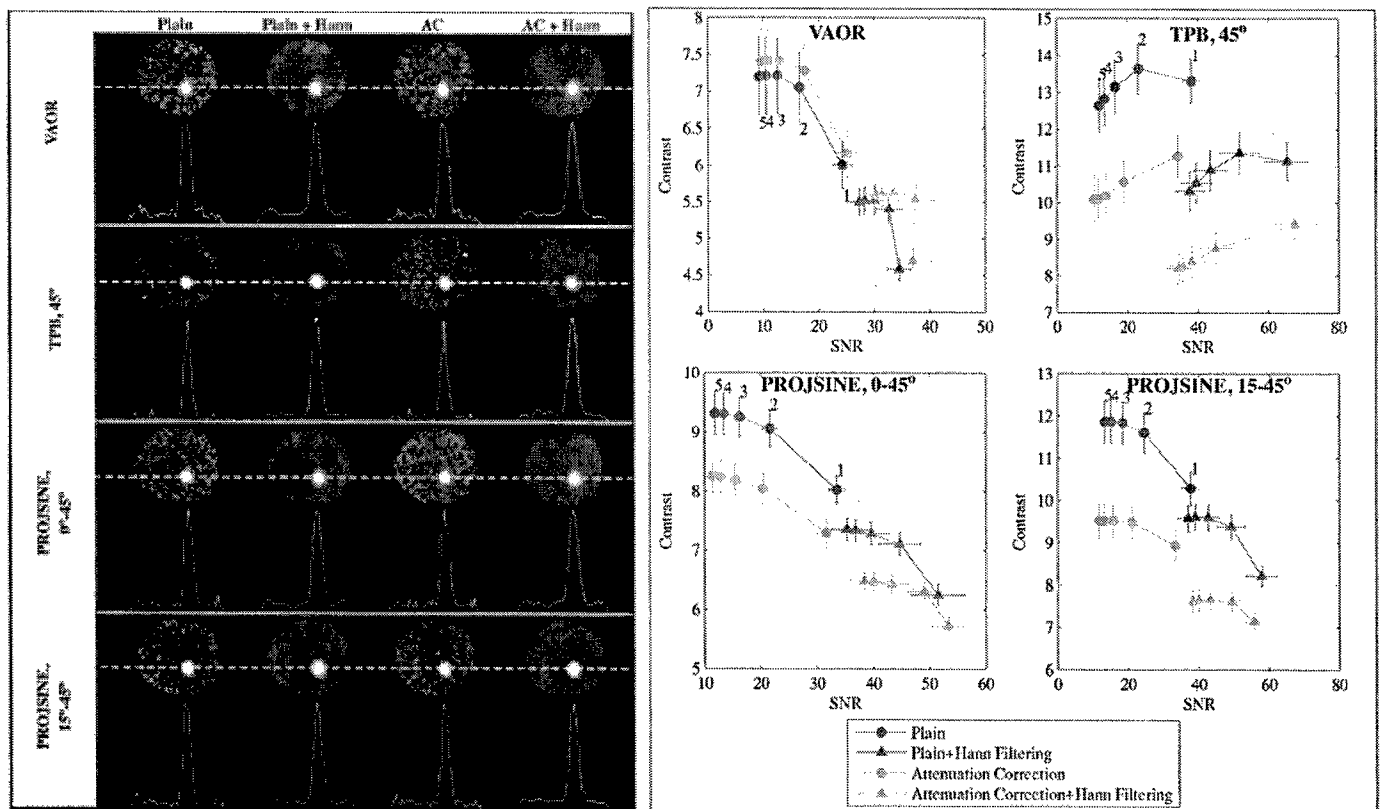


FIG. 6. (LEFT) Images from reconstructed results using various reconstruction techniques (all shown at the 2nd iteration). For the Plain and Attenuation only images, there are 3 summed slices to reduce noise. The filtered images do not have summed slices. Profiles are 9 pixels wide. The dotted line represents the profile center (4 pixels on either side). Plain = no attenuation correction nor Hann Filtering. AC=Attenuation Correction. Hann filter applied at $0.7 \times \text{Nyquist}$.

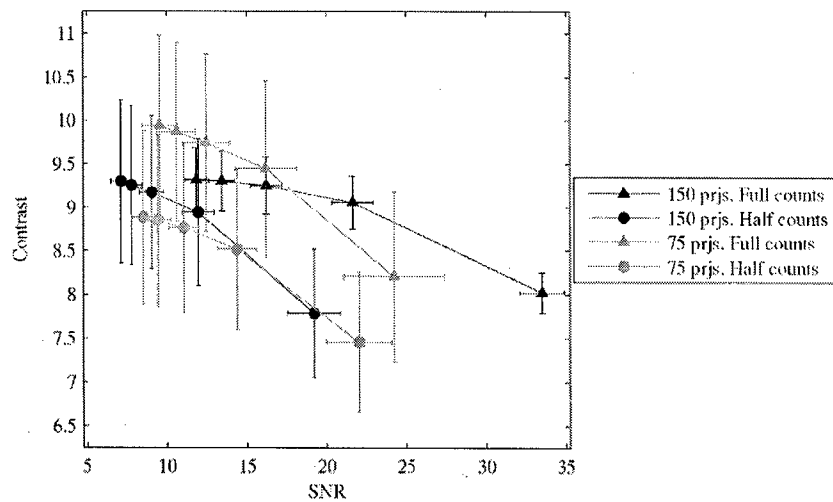


FIG. 7. (LEFT) Contrasts as a function of SNR for the PROJSINE 0-45° orbit, using the full counts as acquired during the scan, and then re-processed with only half of the counts.

Subsequent studies included varying the number of projections and number of counts of the PROJSINE 0-45° orbit, to determine whether the angular sampling plays a key role. Results from these experiments are shown in Fig. 7. "Full counts" utilizes the full number of counts acquired during the scan; "half counts" includes projection files post-processed to reduce the total number of counts by half. To create a projection file with half the number of projections, every other projection angle was written out to a new file. The "half counts" reconstructions provide lower SNRs and contrasts than their "full counts" counterparts, given equal numbers of projections. The comparison we are most interested in is of the 150 projections, half counts to 75 projections, full counts (equivalent total number of counts). The 150 projections, half counts result in lower SNRs and contrasts than the 75 projections, full counts setup. However, at increasing iterations, the SNRs and contrasts are within error bars of each other. Because of the statistical reconstruction algorithm, the angular sampling may not play as large a role as initially anticipated.

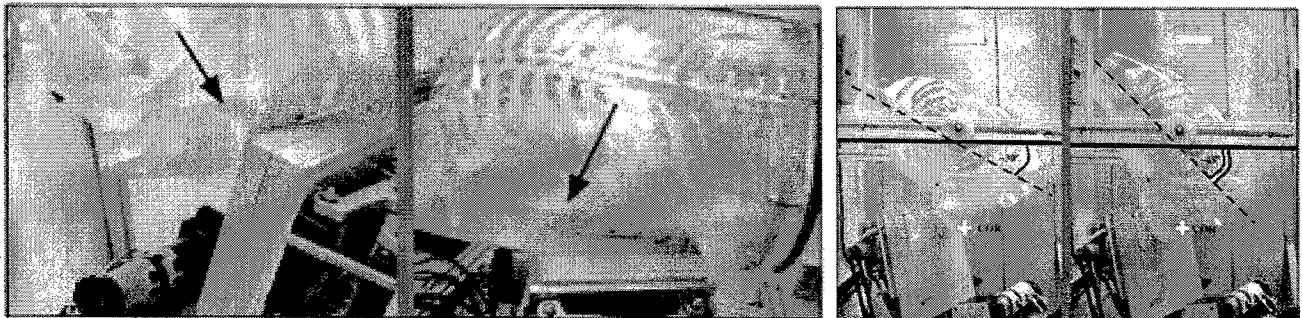


Fig. 8. (LEFT) Two vantages of the positioning problem that arises from the patient's arm. The camera must be at an appropriate polar tilt angle and ROR to get around the arm, which corresponds to an azimuthal location of $\theta \sim 30^\circ$. Arrows point to limit of polar tilt and ROR at this azimuthal location. (RIGHT) Photographs of various degrees of system tilt. (left) 0° system tilt (relative to the horizon; solid lines). The torso is tilted $\sim 30^\circ$ (dashed line) so that the nipple-chest axis is perpendicular to the horizon. (right) 15° system tilt. The torso itself was tilted an additional 15° (dashed line), moving the COR into the outer quadrants of the breast.

In another set of measurements, two system tilt angles were examined to determine whether axillary imaging was achievable in this configuration. With the additional complications that arise with patient positioning, we also wanted to determine whether system tilt would significantly alter acquisition orbit design. Data was initially acquired about suspended anthropomorphic breast and torso phantoms, without a true patient support palette. An example of the positioning problem that arises from the patient's arm is shown in Fig. 8. With multiple degrees of freedom, the parameters we may manipulate to get around the arm include camera tilt and the ROR. For this particular polar tilt, the camera was as close as it could get without hitting the 'patient'. The options are thus (1) to maintain the polar tilt angle but significantly increase the ROR to move the camera completely away from the arm; or, (2) maintain a small ROR by instead increasing the polar tilt. We chose to increasing the polar tilt, resulting in more direct vantages of the heart and liver; however, spatial resolution degradation was minimized. In order to maximize the viewable breast volume, the breast was lowered into the FOV such that the COR was as far into the breast as practicable. The only rotational motion was of the torso itself, with a 15° rotation. Thus, in the case of

increased system tilt, the COR was actually located in the left half of the breast (Fig. 8, right), which we predicted might allow for axillary imaging. Three 130 μ L balloons (Harvard Apparatus, Holliston, MA) (Fig. 9, upper left) were used to simulate uptake in the axillae. Each was filled with $\sim 14 \mu$ Ci of Tc-99m and subsequently placed in wells ~ 2.6 cm deep (Fig. 9, right). In addition, a 2.3 mL lesion (Radiology Support Devices, Newport Beach, CA) was placed near the center of the 935 mL breast phantom, anterior to a large "cold" plug. Projection data were acquired for 20 minutes using both simple and complex 3D orbits; specific parameters for each of four orbits are shown in Fig. 9.



System (Patient) Tilt	Orbit Name	Acronym	Number of Prjs	Polar Tilt Range	ROR Range (min:max) in [cm]
0°	Tilted-Parallel-Beam	TPB	128	45°	3.4
0°	Projected Sine Wave	PROJSINE	135	15-45°	4.0-9.2
15°	Tilted-Parallel-Beam	TPB	128	60°	4.2
15°	Complex Combination of Polynomials	COMPLEX	180	0-70°	3.1-9.4

Fig. 9. (LEFT) Photographs of the phantoms, including: (upper left) Three 130 μ L balloons to simulate uptake in the axillae and one 2.3 mL lesion; (lower left) 935 mL anthropomorphic breast phantom with the 2.3 mL lesion located near the breast center, anterior to a large "cold" plug; (right) Location of the three simulated lymph nodes (breast has been removed). Wells are ~ 2.6 cm deep at each numbered location. (RIGHT) Parameters Used for each Breast-Only Acquisition, with all orbits acquired over a 360° azimuthal range.

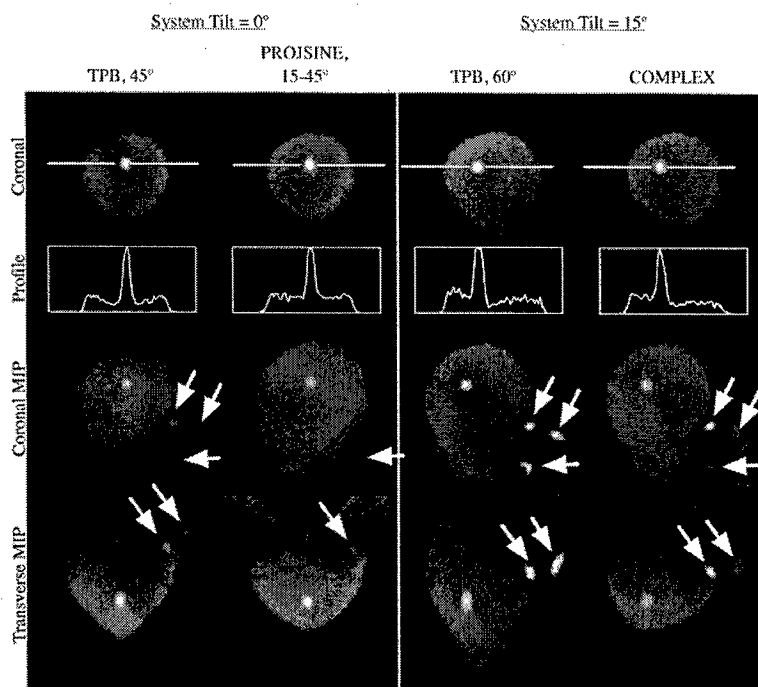


Fig. 10. Images from OSEM reconstructed data (8 subsets, 3 summed slices, 2nd iteration). 2-pixel wide profile drawn through the 2.3 ml lesion. Bottom rows are MIP images through the breast volume, to aid in visualization of the axillae. Axillae are more easily visualized with increased system tilt.

Reconstructed results are shown in Fig. 10. From these preliminary axillary imaging studies, we have shown that axillary imaging is indeed possible, even in the case of 0° system tilt (Fig. 10). Furthermore, the axillae are more clearly visualized when the COR was offset from the nipple-chest axis and a modest amount of system tilt was used (Fig. 10, TPB, 60° and COMPLEX). To simultaneously image both the breast and the axillae, with limited distortion in the breast, an orbit such as COMPLEX could be employed. However, the COMPLEX orbit is not practical because we spent several hours—even with the automated orbit creation code developed—attempting to optimize the orbit considering both the polar tilt and the ROR (to create COMPLEX, ~ 36 hours were required to customize the orbit). A simpler implementation method will need to be developed so that patients will not be required to lie on a table for extended periods of time.

Key Research Accomplishments

Year 2 included tasks 2(b)-3(a) from the original Statement of Work (Appendix A). Task 2 was completed in its entirety. The additional positioning complication of bed shielding was investigated, preliminary measurements of system tilt for axillary imaging were completed, a program was developed to post-process the acquired list-mode data to determine optimal acquisition and system parameters, and Matlab programs were developed to automate orbit creation, including dynamic ROR control. Summarizing specific progress for Task 2:

- Experiments from the effects of additional bed shielding were presented at the *2004 IEEE Nuclear Science Symposium and Medical Imaging Conference*, 16-22 October, Rome, Italy, and published in its associated conference record (Appendix B).
- The results from the preliminary axillary imaging studies were submitted and accepted as an oral presentation to the *2005 IEEE Nuclear Science Symposium and Medical Imaging Conference*, 23-29 October, San Juan, Puerto Rico (Appendix C). An accompanying manuscript will be submitted to the conference record.
- The LMPPro and Matlab programs were developed and have been included within my dissertation. An abstract utilizing results from the LMPPro analysis were submitted and accepted to the *2005 IEEE Nuclear Science Symposium and Medical Imaging Conference* (See Appendix D for submitted abstract), in which I am a co-author.
- Some of the data acquired for task 3(a) was incorporated into a published article, "Evaluation of Fully 3D Emission Mammotomography with a Compact Cadmium Zinc Telluride Detector," *IEEE Transactions on Medical Imaging*, 2005. See attached article in Appendix E for details.

Related:

- Results from this work were included in my preliminary proposal, "Development and Evaluation of a Dedicated Emission Mammotomography System," which was accepted by my dissertation committee on September 16, 2004.
- Our lab grew by three graduate students this year, beginning in September 2004. I have had extensive opportunities to mentor, train, and educate Priti Madhav, Dominic Crotty, and Spencer Cutler, for whom we have been co-authors on submitted and accepted abstracts to the *2005 IEEE Nuclear Science Symposium and Medical Imaging Conference*. A post-doctoral student, Dr. Esther Dura, also joined the lab in June 2005. Already, we have interacted many times, exchanging ideas about image registration of the functional and structural reconstructed images obtained from our systems.
- I have been able to apply knowledge learned about unique 3D acquisition orbits from this work to X-ray computed mammotomography, resulting in several published conference proceedings of the SPIE. In addition, I have also contributed to a comparison of mammotomography, which utilized the arbitrary orbits, to scintimammography.
- I am currently in the process of writing my dissertation, which I expect to defend within the next few months. All of the results from this grant have been included within my thesis.

Reportable Outcomes

Peer-reviewed articles

C.N. Brzymialkiewicz, M.P. Tornai, R.L. McKinley, and J.E. Bowsher, "Evaluation of Fully 3D Emission Mammotomography with a Compact Cadmium Zinc Telluride Detector," *IEEE Trans. on Med. Imag.* vol. 24, no. 7, pp. 868-877, 2005.

M.P. Tornai, C.N. Brzymialkiewicz, M.L. Bradshaw, J.E. Bowsher, B.E. Patt, J.S. Iwanczyk, J. Li, and L.R. MacDonald, "Comparison of Compact Gamma Cameras with 1.3mm and 2.0mm Quantized Elements for Dedicated Emission Mammotomography," *IEEE Trans. Nucl. Sci.* (In Press).

Presentations, Published Abstracts, and Published Proceedings:

- C.N. Brzymialkiewicz, M.P. Tornai, R.L. McKinley, and J.E. Bowsher, "3D Data Acquisition Sampling Strategies for Dedicated Emission Mammotomography for Various Breast Sizes," Presented at the 2004 IEEE NSS/MIC, 16-22 October, Rome, Italy, and published in the 2004 IEEE NSS/MIC Conference Record, vol. 4, pp. 2596 – 2600.
- M.P. Tornai, C.N. Brzymialkiewicz, and S.J. Cutler and P. Madhav, "Comparison of scintimammography and dedicated emission mammotomography," Presented at the 2004 IEEE NSS/MIC, 16-22 October, Rome, Italy, and published in the 2004 IEEE NSS/MIC Conference Record, vol. 5, pp. 2818 – 2822.
- M.P. Tornai, R.L. McKinley, C.N. Brzymialkiewicz, P. Madhav, S.J. Cutler, D.J. Crotty, J.E. Bowsher, E. Samei and C.E. Floyd, "Design and Development of a Fully-3D Dedicated X-ray Computed Mammotomography (CmT) System," Presented at the 2005 SPIE Medical Imaging Conference, San Diego, CA, 12 – 17 Feb. 2005, and published in *Proc. SPIE: Physics of Medical Imaging*, 5745(1):189-197.
- C.N. Brzymialkiewicz and M.P. Tornai, "Novel Three-dimensional Acquisition Orbits with a Dedicated Emission Mammotomography System," Presented at the DOD Era of Hope Conference, 8-11 June 2005, Philadelphia, PA.
- C.N. Brzymialkiewicz, R.L. McKinley, and M.P. Tornai, "Initial Patient Results from Dedicated Emission Mammotomography," Abstract submission accepted to the 2005 Nucl. Sci. Symp. & Med. Imag. Conf., San Juan, Puerto Rico, 23-29 Oct. 2005.
- D.J. Crotty, C.N. Brzymialkiewicz, R.L. McKinley, and M.P. Tornai, "Optimizing Orientation of SPECT and CT Detectors Through Quantification of Cross Contamination in a Dual Modality Mammotomography System," Abstract submission accepted to the 2005 Nucl. Sci. Symp. & Med. Imag. Conf., San Juan, Puerto Rico, 23-29 Oct. 2005.
- S.J. Cutler, C.N. Brzymialkiewicz, and M.P. Tornai, "Investigating the Effects of Energy Resolution in Dedicated Emission Mammotomography," Abstract submission accepted to the 2005 Nucl. Sci. Symp. & Med. Imag. Conf., San Juan, Puerto Rico, 23-29 Oct. 2005.
- P. Madhav, C.N. Brzymialkiewicz, J.E. Bowsher, and M.P. Tornai, "A Novel Way to Characterize the MTF in 3D for Quantized SPECT Cameras Having Arbitrary Trajectories," Abstract submission accepted to the 2005 Nucl. Sci. Symp. & Med. Imag. Conf., San Juan, Puerto Rico, 23-29 Oct. 2005.

Conclusions

From these studies utilizing complex 3D acquisition orbits, we have demonstrated that lesions near the chest wall can be visualized for both large and small sized breasts, and further, that axillary imaging is possible with our system. Acquisition parameters were also evaluated to determine an optimal imaging protocol for potential future patient studies. Given the very similar SNR and contrast values for all examined orbits, it would seem that other factors are more important in determining sampling strategy, including the reconstructed breast and lesion shape, visualization of the area near the chest wall (i.e. lesion location), and area of the reduced-artifact region of the breast. However, one could utilize a different sampling strategy depending on the imaging task. Future work includes the addition of a patient bed, which is expected to complicate positioning even further, and which may or may not include lead lining pending further studies.

References

- [1] C.N. Archer, M.P. Tornai, J.E. Bowsher, S.D. Metzler, B.C. Pieper, and R.J. Jaszczyk. Implementation and initial characterization of acquisition orbits with a dedicated emission mammotomograph. *IEEE Trans. Nucl. Sci.*, 50(3):418–420, 2003.
- [2] M.P. Tornai, J.E. Bowsher, C.N. Archer, J. Peter, R.J. Jaszczyk, L.R. MacDonald, B.E. Patt, and J.S. Iwanczyk. A 3d gantry single photon emission tomograph with hemispherical coverage for dedicated breast imaging. *Nucl. Inst. & Meth. Phys. Res. A*, A497(1):157–167, 2003.
- [3] M. B. Williams, D. Narayanan, M. J. More, P. J. Goodale, S. Majewski, and D. A. Kieper. Analysis of position-dependent Compton scatter in scintimammography with mild compression. *IEEE Trans. Nucl. Sci.*, 50(5):1643–1649, 2003.

- [4] B.C. Pieper, J.E. Bowsher, M.P. Tornai, C.N. Archer, and R.J. Jaszcak. Parallel-beam tilted-head analytic SPECT reconstruction: Derivation and comparison with OSEM. *IEEE Trans. Nuc. Sci.*, 49:2394–2400, 2002.
- [5] S.D. Metzler, J.E. Bowsher, M.P. Tornai, B.C. Pieper, J. Peter, and R.J. Jaszcak. SPECT breast imaging combining horizontal and vertical axes of rotation. *IEEE Trans. Nuc. Sci.*, 49(1):31–36, 2002.
- [6] S. D. Metzler, J. E. Bowsher, and R. J. Jaszcak. Geometrical similarities of the Orlov and Tuy sampling criteria and a numerical algorithm for assessing sampling completeness. *IEEE Trans. Nucl. Sci.*, 50(5):1550–1555, 2003.

APPENDIX A

Statement of Work

- Task 1* Implement and characterize modified basis set of orbits (Months 1-5):
- a. Implement dynamic ROR capability in hardware to enable fully computer controlled gantry. (Month 1)
 - b. Program gantry for: modified circle-plus-arc orbit with different arc locations, cloverleaf orbit. (Month 2)
 - c. Perform phantom measurements using modified orbits and evaluate projection data for signal-to-noise (SNR), contrast, and lesion visualization improvement. (Months 2-5).
- Task 2* Development and investigation of novel orbits (Months 5-22):
- a. Use Monte Carlo and Analytic computer simulations, including computations of Orlov Volumes, to develop novel orbits for various breast shapes and sizes through parameters of viewable breast volume, radius-of-rotation (ROR), camera tilt angle (to minimize background contamination). (Months 5-12)
 - b. Investigate the effect of additional bed shielding on positioning of the compact gamma camera. (Months 12-15)
 - c. Investigate acquisition and system parameters, including system tilt for axillary imaging, total number of projections and hence angular sampling, and distribution of the scan time. (Months 15-18)
 - d. Develop software to automate process of orbit creation, utilizing dynamic ROR control. (Months 18-22)
- Task 3* Experimental evaluation of orbits (Months 22-36):
- a. Acquire experimental projection data using cold rod and cold disk phantoms for resolution and sampling characterization, respectively. (Months 22-29)
 - b. Utilize anthropomorphic breast containing lesions and torso phantoms to acquire projection data. Analyze reconstructed images for contrast, signal-to-noise ratio, lesion detectability, and extent of artifacts caused by torso contamination. (Months 29-36)

3D Data Acquisition Sampling Strategies for Dedicated Emission Mammotomography for Various Breast Sizes

Caryl N. Brzymialkiewicz, *Member, IEEE*, Martin P. Tornai, *Member, IEEE*,
Randolph L. McKinley, *Member, IEEE*, Spencer J. Cutler, *Member, IEEE*, and James E. Bowsher, *Member, IEEE*

Abstract—The dedicated emission mammotomography system developed in our lab is in preparation for initial patient studies. As a preliminary step, we evaluate the effect of breast size and lesion location on this paradigm. The hemispherical positioning gantry allows ample flexibility in sampling a pendant, uncompressed breast. Recently acquired, realistic anthropomorphic torso (which includes the upper portion of the arm) and breast phantoms emphasize the necessity of employing unique camera trajectories (orbits) rather than simple VAOR camera trajectories. Several novel 3D orbits have been implemented with fully contoured radius-of-rotation capability to compensate for the positioning demands that are required for different breast sizes. While a general orbit design may remain the same between two different breasts, the absolute polar tilt range and ROR range may vary. We have demonstrated that with increased polar camera tilt, employing 3D data acquisition camera trajectories, lesions near the chest wall can be visualized for both large and small sized breasts.

Index Terms—Breast imaging, emission mammotomography, single photon emission computed tomography, three-dimensional orbits, CZT detector

I. INTRODUCTION

Our group has previously investigated several parallel-beam fully 3D acquisition orbits about a pendant breast, both with and without additional torso backgrounds. Results thus far have shown that no single camera trajectory will equally optimize image quality for various lesion sizes located in different areas of the breast [1]–[3]. However, some orbits may be more easily adaptable to varieties of breast shapes and sizes. For this set of experiments, we focus on three specific orbit types: Vertical Axis of Rotation (VAOR), Tilted Parallel Beam (TPB), and Projected Sine Wave (PROJSINE).

The dedicated emission mammotomography system we have been developing in our lab is in preparation for initial patient studies. As a preliminary step, we evaluate the effect of various breast sizes and lesion location on this paradigm. The hemispherical positioning gantry allows ample flexibility in sampling a pendant, uncompressed breast. The gantry itself

has been described in detail elsewhere [1], [2]. The compact gamma camera currently attached to the system is the CZT-based Lumagem 3200-S (*Gamma Medica*, Northridge, CA) with 2.5 mm² discrete pixels, with a measured energy resolution of 6.1% FWHM at 140 keV and sensitivity of 37.9 cps/MBq.

Key benefits of utilizing 3D acquisition orbits include the ability to contour the breast, reducing distance-dependent spatial resolution limitations, and the capability of imaging further into the breast, near the chest wall, by employing camera polar tilt. Recently acquired, realistic anthropomorphic torso (which includes the upper portion of the arm) and breast phantoms emphasize the necessity of employing unique camera trajectories (orbits) rather than simple VAOR camera trajectories. For a simple circular orbit (VAOR, for example, with 360° azimuthal rotation, no polar camera tilt), the amount of viewable breast volume is limited by the placement of the camera next to the torso. Due to physical limitations, the tissue immediately anterior to the chest wall is not within the field-of-view (FOV) (Fig. 1, VAOR, white arrow). By simply increasing the camera polar tilt angle to 45°, the center-of-rotation (COR) moves further into the breast as compared to VAOR, thus allowing the entire volume to be viewed. However, artifacts result from the incompletely sampled TPB orbit. Hence, more complex 3D camera trajectories which more-nearly-completely sample the breast while minimizing direct lines-of-sight of the heart and liver are desired. Furthermore, complex 3D orbits can be designed to avoid physical limitations imposed by the patient (e.g. arms) or bed.

One type of complex 3D orbit investigated in this work is the PROJSINE (Fig. 2), which is a sine wave projected onto the hemisphere, where the number of ‘lobes’ and the polar tilt range can be varied. Three lobes minimize the number of times the camera must reach $\phi=0^\circ$ (a position that requires larger radius-of-rotation (ROR)). Two variations of PROJSINE were examined within this work, one going from 0° to 45°, and the other from 15° to 45°. By allowing the camera to start at a polar tilt angle of 15° rather than 0°, the COR moves further into the breast, yielding an increased viewable breast volume including imaging near the chest wall, and decreased maximum ROR.

Manuscript submitted November 1, 2004. This work was supported by the National Institutes of Health under grant R01-CA96821 and by U.S. Army Grant No. DAMD17-03-1-0558.

C.N. Brzymialkiewicz, M.P. Tornai, R.L. McKinley, and S.J. Cutler are with the Departments of Biomedical Engineering and Radiology; J.E. Bowsher is with the Department of Radiology, Duke University Medical Center, Durham, NC 27710 USA (email:cnb3@duke.edu).

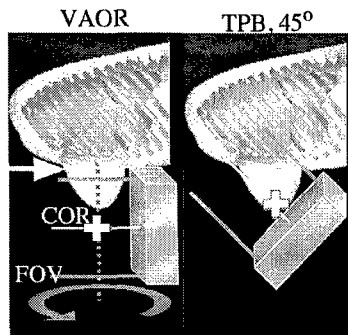


Fig. 1. COR moves further into the breast with increased camera polar tilt, allowing for imaging of the breast near the chest wall.

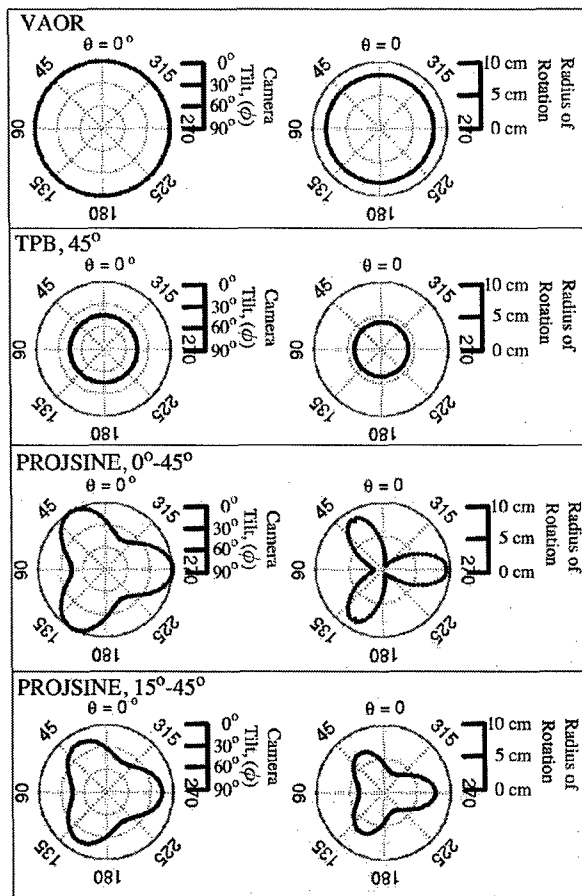


Fig. 2. Within each box, the left plot shows polar camera tilt as a function of the azimuthal angle; the right plot shows the radius of rotation, shown here for the 1060 ml breast phantom.

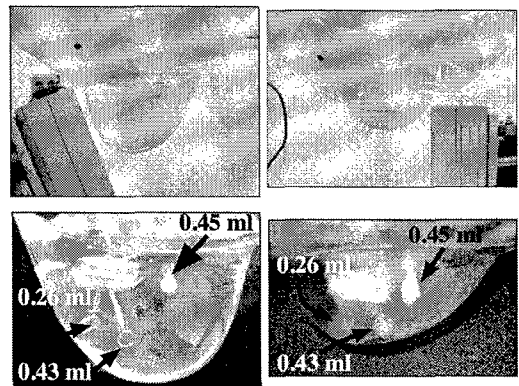


Fig. 3. Photographs of the 1060 ml (left) and 325 ml (right) anthropomorphic breast phantoms. Dimensions of the breast phantoms (given in [cm] as: superior-inferior x nipple-chest x medial-lateral) for the 1060 ml phantom: 15.9 x 12.1 x 17.8; for the 325 ml phantom: 12.9 x 4.4 x 13.5. Two sets of embedded lesions were inserted into each phantom, with lesion sizes as labeled.

TABLE I

PARAMETERS USED FOR EACH BREAST-ONLY ACQUISITION, WITH ALL ORBITS ACQUIRED OVER A 360° AZIMUTHAL RANGE (θ).

Orbit	ϕ (Range, min:max)	325 ml		1060 ml	
		COR Location (relative to the nipple) [‡] (cm)	ROR [†] (Range, min:max) (cm)	COR Location (relative to the nipple) [‡] (cm)	ROR [†] (Range, min:max) (cm)
VAOR	0°	-5.5	6.1	-1.0	8.0
TPB	45°	-2.6	1.1	1.7	4.0
PROJSINE	0 : 45°	-5.5	0.0 : 7.0	-1.0	0.8 : 9.4
PROJSINE	15 : 45°	-2.6	0.6 : 5.5	1.7	3.1 : 7.7

[‡]Negative values indicate CORs outside and below the nipple.

[†]ROR defined as the distance from the center of the detector to the COR.

II. METHODS

A. Isolated Breast Phantom

Two custom breast phantoms (Fig. 3) (Radiology Support Devices, Newport Beach, CA) were used in conjunction with the 3D orbits. Three lesions were placed in each breast (Fig. 3); one 0.45 ml catheter balloon lesion (Harvard Apparatus, Holliston, MA) was glued onto the anterior chest wall, one 0.43 ml acrylic sphere lesion (Data Spectrum Corp., Hillsborough, NC) was placed as centrally in the breast as possible, and one 0.26 ml lesion (Data Spectrum Corp.) was placed laterally within the breast. The absolute activity for the lesions in the 325 ml breast was 21.1 $\mu\text{Ci/ml}$; in the 1060 ml breast, the lesion activity was 20.0 $\mu\text{Ci/ml}$. Ten minute scans were performed, with acquisition times increased in subsequent scans to account for radioactive decay. A $\pm 8\%$ energy window about the 140 keV photopeak of Tc-99m was used. Three lesion:breast concentration ratios were used, including 10:1, 6:1, and 3:1. Specific orbit parameters used for each scan are given in Table I. VAOR and TPB each had 128 projections; the PROJSINE orbits had 150 projections.

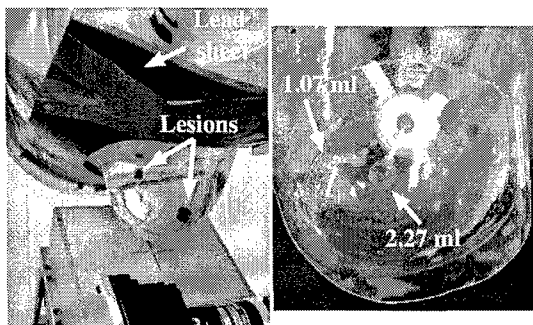


Fig. 4. Photographs of: (left) 1060 ml breast phantom attached to the torso, with a lead sheet to shield 'patient'; (right) One set of embedded lesions were inserted, with lesion sizes as labeled.

TABLE II
PARAMETERS USED FOR EACH BREAST+ FILLED TORSO ACQUISITION,
WITH ALL ORBITS ACQUIRED OVER A 360° AZIMUTHAL RANGE (θ).

Orbit	ϕ (Range, min:max)	COR Location (relative to the nipple) [‡] (cm)	ROR [†] (Range, min:max) (cm)
VAOR	0°	-1.0	8.2 : 9.4
TPB	45°	1.7	3.3 : 4.1
PROJSINE	0 : 45°	-1.0	1.3 : 9.4
PROJSINE	15 : 45°	1.7	3.1 : 7.7

[‡]Negative values indicate CORs outside and below the nipple.

[†]ROR defined as the distance from the center of the detector to the COR.

B. Breast Phantom with Filled Torso Background

Two lesions were embedded in the 1060 ml breast phantom, which was then attached to a filled anthropomorphic torso phantom that included a heart, lungs, and liver (RSD) (Fig. 4). A 1.07 ml (~1.27 cm diam.) lesion was placed near the chest wall; a 2.27 ml (~1.6 cm diam.) lesion (RSD) was placed in the center of the breast. The absolute lesion activity was 10.4 μ Ci/ml; the lesion:torso-and-breast:heart-and-liver concentration ratio was 11:1:10. Projection data were acquired for 20 minutes, with subsequent scans adjusted to compensate for radioactive decay. A $\pm 8\%$ energy window was again used. Scans were acquired with and without the 1/4" lead sheet, which was securely taped to the phantom to simulate shielding of the 'patient' along with the fully pendant exposed breast of interest.

C. Image Reconstruction and ROI Analysis

Images were reconstructed from projection data using an OSEM algorithm with ray-tracing capability, with 8 subsets, 5 iterations, and calculated attenuation correction assuming a uniform emission volume [4], [5]. For ease of display only (because the lesions' locations are through various planes of the breast), Maximum Intensity Projections (MIP) are used to summarize the reconstructed data. Regions-of-interest (ROIs) were drawn in the reconstructed images both inside the lesions and circumferentially about each lesion in the breast background. A 9-pixel ROI was drawn inside and about the 0.43 ml lesion

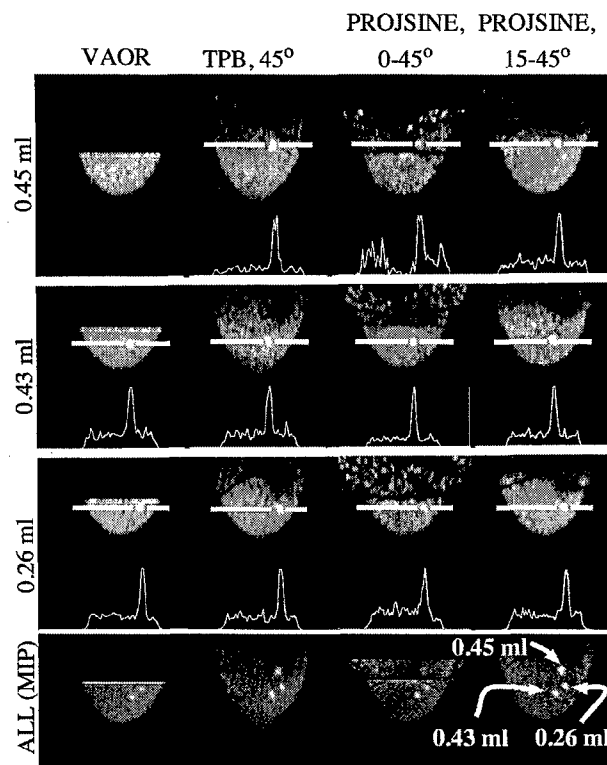


Fig. 5. Top three rows are images obtained from reconstructed data (OSEM, 2.5mm voxels, 2nd iteration shown, attenuation correction, 3 summed slices to reduce noise) for the 1060 ml breast phantom, with a 10:1 concentration ratio, and showing all lesions. Note that the 0.45 ml lesion (located near the chest wall) is not visible with VAOR. Bottom row is the Maximum Intensity Projection (MIP) through the breast volume.

for the breast only studies; a 9-pixel ROI was drawn inside and about the 2.27 ml lesion for the breast+torso studies.

The SNR was measured as the difference in mean pixel values of the lesion and breast background, divided by the standard deviation of the uniform background ($(ROI_{lesion} - ROI_{breast})/\sigma_{breast}$), where ROI_{lesion} and ROI_{breast} are the mean values of the counts within each respective region and σ_{breast} is the standard deviation of the uniform breast background. Lesion contrast is defined as the signal difference divided by the background signal ($(ROI_{lesion} - ROI_{breast})/ROI_{breast}$).

III. RESULTS & DISCUSSION

As seen in Fig. 5, the lesion nearest the chest wall (0.45 ml) cannot be seen with VAOR. This lesion is not visible for the 1060 ml breast nor the 325 ml breast with VAOR (Figs. 6 and 7), a result of the physical limitation of placing the detector near the torso. For the 3:1 concentration ratio, none of the lesions were visible in the 1060 ml breast (Fig. 6), while all lesions were visible in the 325 ml breast phantom (Fig. 7) (with the exception of the chest wall lesion using VAOR). This may be expected given the increased ROR with the larger breast and increased amount of attenuating tissue.

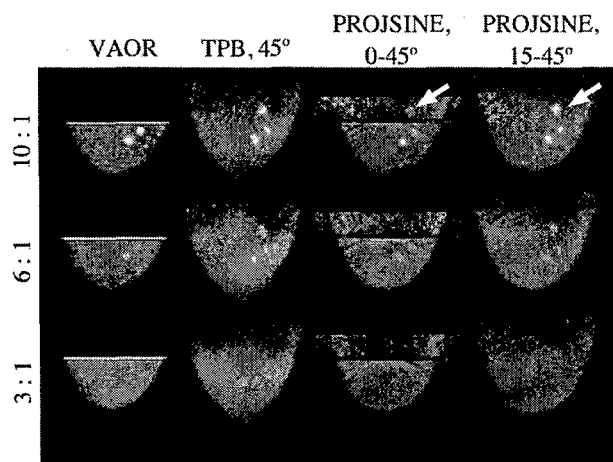


Fig. 6. Maximum Intensity Projections (Sagittal view) for the 1060 ml breast for all concentration ratios and orbits, as labeled. White arrows point to the lesion nearest the chest wall, which is more easily visualized with PROJSINE 15-45°.

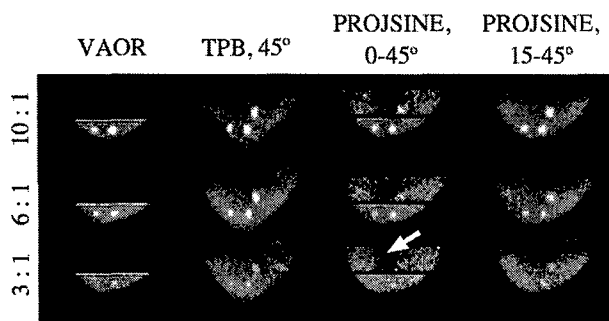


Fig. 7. Maximum Intensity Projections (Sagittal view) for the 325 ml breast for all concentration ratios and orbits, as labeled. White arrow points to cold area, due to nylon screw.

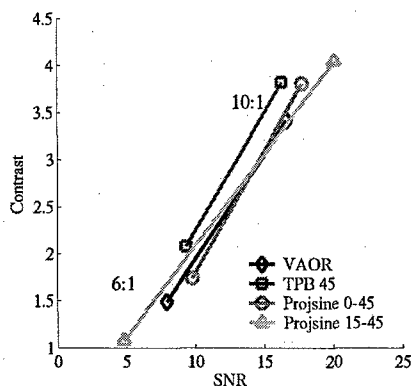


Fig. 8. SNR and Contrast results for the centrally-located 0.43 ml lesion (2nd iteration) embedded in the 1060 ml breast.

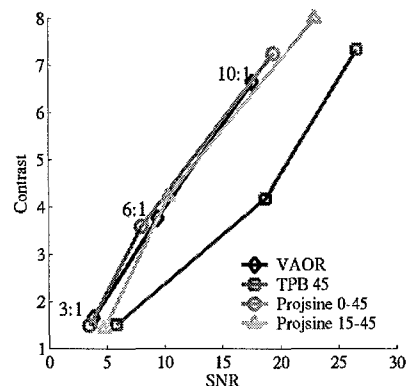


Fig. 9. SNR and Contrast results for the centrally-located 0.43 ml lesion (2nd iteration) embedded in the 325 ml breast.

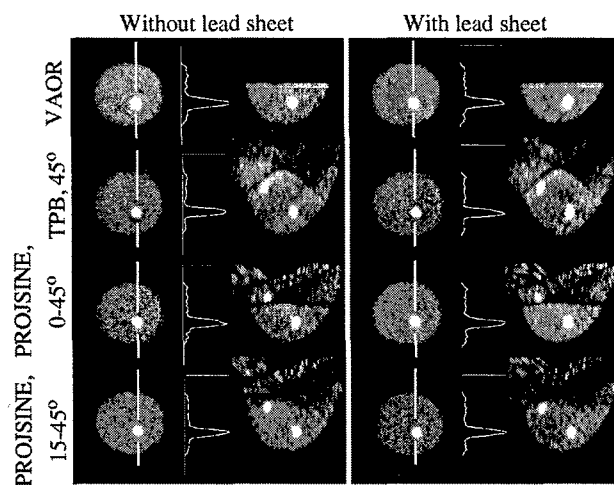


Fig. 10. Images from reconstructed data (OSEM, 2.5mm voxels, 2nd iteration shown, attenuation correction, 3 summed slices, transaxial view) for the 1060 ml breast and filled torso, with and without the lead sheet. Similar to the breast-only studies, the smaller lesion is not visible with VAOR and artifacts move further into the breast for the PROJSINE 15-45° case as compared to PROJSINE 0-45°.

As expected, the TPB orbit yields a distorted breast shape due to incomplete sampling. Indeed, the lesions are also somewhat distorted with TPB. The more-nearly-completely sampled PROJSINE orbits recovers the breast shape more accurately than TPB, however, artifacts near the chest wall are still visible. Note that there is no activity "above" the breast volume (i.e. in the chest wall region), yet because of the sampling, in which all activity is not within the FOV for all vantages of the camera, the reconstructed images have incorrectly placed activity. By sacrificing some polar sampling of PROJSINE by starting at 15° polar tilt rather than 0°, the COR moves further into the breast, thus increasing the reduced-artifact region of the breast volume and allowing easier visualization of the lesion near the chest wall (Fig. 6, white arrows).

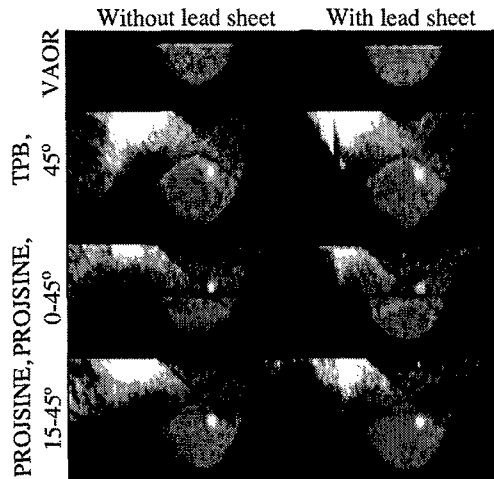


Fig. 11. Images from reconstructed data (OSEM, 2.5 mm voxels, 2nd iteration shown, attenuation correction, summed slices, sagittal view) for the 1060 ml breast and filled torso, with and without the lead sheet. More background contamination is visible without the lead sheet; increased tilt views the heart and liver more directly.

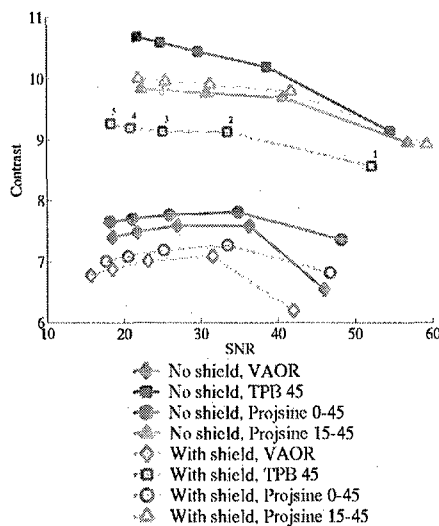


Fig. 12. SNR and Contrast results for the 2.27 ml lesion. Iterations labeled next to TPB 45°. Patient shielding yields slightly lower SNR and contrast values.

For each concentration ratio, all orbits yield similar SNR and contrast values for the 1060 ml breast phantom (Fig. 8); for the 325 ml breast, TPB 45° seems to outperform the others (Fig. 9).

Reconstructed results for the shielding experiments are shown in Figs. 10 and 11. No patient shielding yields slightly higher SNR and contrast values than with patient shielding (Fig. 12). We intend to repeat the study with breast-only filled measurements, prior to attaching the breast to the filled torso phantom.

IV. CONCLUSIONS

Orbits that include increased camera polar tilt angles allow for imaging of lesions near the chest wall and/or smaller breasts. Because previous studies have suggested the tomographic sampling criteria for completeness may not be as strict as initially anticipated, we relaxed the restrictions on the camera polar tilt. This allowed the COR to move further into the breast, which increased the reduced-artifact region of the breast, thus allowing easier visualization of lesions near the chest wall. These studies were intentionally not performed with clinical count densities since we wanted to determine the effect of the sampling strategy itself. Given the very similar SNR and contrast values for all examined orbits, it would seem that other factors are more important in determining sampling strategy, including the reconstructed breast and lesion shape, visualization of the area near the chest wall (i.e. lesion location), and area of the reduced-artifact region of the breast. However, one could utilize a different sampling strategy depending on the imaging task. For example, if a lesion is suspected near the chest wall, then to confirm diagnosis of a lesion in that region one may utilize more camera tilt; to determine whether a smaller lesion and/or lesion of low radiopharmaceutical uptake is present anywhere in the breast, an orbit such as TPB, with its decreased ROR, may be more appropriate. Further studies will be necessary to fully characterize the sensitivity of the system in various breast sizes.

V. ACKNOWLEDGMENTS

The authors thank K. Parnham (*Gamma Medica*) for assistance with camera operation.

REFERENCES

- [1] M. P. Tornai, J. E. Bowsher, C. N. Archer, J. Peter, R. J. Jaszcak, L. R. MacDonald, B. E. Patt, and J. S. Iwanczyk, "A 3D gantry single photon emission tomograph with hemispherical coverage for dedicated breast imaging," *Nucl. Inst. Meth.*, vol. A497, no. 1, pp. 157-167, 2003.
- [2] C. N. Archer, M. P. Tornai, J. E. Bowsher, S. D. Metzler, B. C. Pieper, and R. J. Jaszcak, "Implementation and initial characterization of acquisition orbits with a dedicated emission mammotomograph," *IEEE Trans. Nucl. Sci.*, vol. 50, no. 3, pp. 418-420, 2003.
- [3] C.N. Brzymialkiewicz, M.P. Tornai, R.L. McKinley, and J.E. Bowsher, "Evaluation of Fully 3D Emission Mamotomography with a Compact Cadmium Zinc Telluride Detector", Submitted to *IEEE Transactions on Medical Imaging*, 15 July 2004.
- [4] H.M. Hudson and R.S. Larkin, "Accelerated image reconstruction using ordered subsets of projection data," *IEEE Trans. Medical Imaging*, vol. 13, no. 4, pp. 601-609, 1994.
- [5] J. E. Bowsher, D. R. Gilland, C. E. Floyd, R. J. Jaszcak, V. E. Johnson, and R. E. Coleman, "Three dimensional iterative reconstruction for SPECT," *J. Nucl. Med.*, vol. 33, p. 879, 1992 (abstract).

APPENDIX C

Initial Patient Results from Dedicated Emission Mammotomography

C. N. Brzymialkiewicz^{1,2}, R. L. McKinley^{1,2}, M. P. Tornai^{1,2}

¹*Radiology, Duke University, Durham, NC, USA*

²*Biomedical Engineering, Duke University, Durham, NC, USA*

A patient bed was recently developed and subsequent modifications made for 3D, pendant breast imaging with a dedicated emission mammotomography system that incorporates a discretized 16x20cm² CZT gamma camera with 2.5mm pixels. Goals for these experiments include: (1) designing acquisition orbits to minimize effects from complications that arise with patient positioning; (2) determining the optimal amount of system tilt to adequately image the breast; (3) determining whether axillary imaging is possible in this configuration. Data was initially acquired with Tc-99m filled anthropomorphic breast and torso phantoms for each of three cases: activity in the breast only; activity in the breast and torso; activity in both, with lead shielding placed on the pallet (to mimic an intended custom-designed lead-lined pallet). Projection data were acquired for 20 minutes using both simple and complex 3D orbits. Optimal positioning parameters determined from the phantom studies are then applied to a patient scan. We have found that acquisition orbits can be modified to accommodate the bed's physical hindrances and still recover most of the volume of interest, while minimizing distortion and artifacts in the reconstructed images. Initial patient results with the mammotomography system are presented. Overall, the results indicate this approach could be a beneficial diagnostic tool to aid in the characterization of lesions.

This work was funded by DOD DAMD17-03-1-0558, NIH R01-CA96821, and in part by W81XWH-05-1-0280.

Submitted to the
2005 Nuclear Science Symposium & Medical Imaging Conference
San Juan, Puerto Rico
23-29 October, 2005

APPENDIX D

Investigating the Effects of Energy Resolution in Dedicated Emission Mammotomography

Spencer J. Cutler^{1,2}, Caryl N. Brzymialkiewicz^{1,2}, Martin P. Tornai^{1,2}

¹ Department of Radiology, Duke University, Durham, NC

² Department of Biomedical Engineering, Duke University, Durham, NC

This study probes the recent debate over the necessity for good energy resolution for breast lesion imaging with dedicated single photon emission mammotomography, an uncompressed breast, fully-3D imaging modality developed in our lab. The system consists of a commercial, discretized CZT gamma camera having 6.7% FWHM energy resolution (at 140keV) and intrinsic spatial resolution corresponding to the 2.5mm square pixel, and is used on a fully-3D positioning gantry. The energy resolution on this high performance imaging device can be effectively degraded by using wider energy windows in list mode acquired data. Multiple 3D orbits about Tc-99m filled anthropomorphic breast and torso phantoms are acquired. The full spectrum list mode data files were multiply processed to obtain images of varying energy window widths (from symmetric 6% to an asymmetric 18% (-12+6)) but with the same projection image count density. Counts were randomly subsampled from the entire list mode data set in order to maintain an equivalent level of noise. The data was then reconstructed using OSEM for various iterations. Regions of interest were drawn in and about spherical lesions of different volumes to determine signal-to-noise ratios and contrasts for each iteration. Results clearly illustrate both visual and quantitative differences between the various energy windows, with smaller energy windows (better ERes) having better image quality. Results for clinical count densities are also investigated.

This work was funded by NIH R01-CA96821, in part by DOD DAMD17-03-1-0558, and Duke BME.

Submitted to the
2005 Nuclear Science Symposium & Medical Imaging Conference
San Juan, Puerto Rico
23-29 October, 2005

Evaluation of Fully 3-D Emission Mammotomography With a Compact Cadmium Zinc Telluride Detector

Caryl N. Brzymialkiewicz*, *Member, IEEE*, Martin P. Tornai, *Member, IEEE*, Randolph L. McKinley, *Member, IEEE*, and James E. Bowsher, *Member, IEEE*

Abstract—A compact, dedicated cadmium zinc telluride (CZT) gamma camera coupled with a fully three-dimensional (3-D) acquisition system may serve as a secondary diagnostic tool for volumetric molecular imaging of breast cancers, particularly in cases when mammographic findings are inconclusive. The developed emission mammotomography system comprises a medium field-of-view, quantized CZT detector and 3-D positioning gantry. The intrinsic energy resolution, sensitivity and spatial resolution of the detector are evaluated with Tc-99m (140 keV) filled flood sources, capillary line sources, and a 3-D frequency-resolution phantom. To mimic realistic human pendant, uncompressed breast imaging, two different phantom shapes of an average sized breast, and three different lesion diameters are imaged to evaluate the system for 3-D mammotomography. Acquisition orbits not possible with conventional emission, or transmission, systems are designed to optimize the viewable breast volume while improving sampling of the breast and anterior chest wall. Complications in camera positioning about the patient necessitate a compromise in these two orbit design criteria. Image quality is evaluated with signal-to-noise ratios and contrasts of the lesions, both with and without additional torso phantom background. Reconstructed results indicate that 3-D mammotomography, incorporating a compact CZT detector, is a promising, dedicated breast imaging technique for visualization of tumors <1 cm in diameter. Additionally, there are no outstanding trajectories that consistently yield optimized quantitative lesion imaging parameters. Qualitatively, imaging breasts with realistic torso backgrounds (out-of-field activity) substantially alters image characteristics and breast morphology unless orbits which improve sampling are utilized. In practice, the sampling requirement may be less strict than initially anticipated.

Index Terms—Breast imaging, CZT detector, emission imaging, mammotomography, single photon emission computed tomography, SPECT, three-dimensional orbits.

Manuscript received January 13, 2005; revised May 25, 2005. This work was supported in part by the National Institutes of Health (NIH) under Grant R01-CA96821 and in part by the U.S. Army under Grant DAMD17-03-1-0558. The Associate Editor responsible for coordinating the review of this paper and recommending its publication was J. Basilion. Asterisk indicates corresponding author.

*C. N. Brzymialkiewicz is with the Multi-Modality Imaging Laboratory, Departments of Biomedical Engineering and Radiology, Duke University Medical Center, DUMC-3949, Durham NC 27710 USA (e-mail: cnb3@duke.edu).

M. P. Tornai and R. L. McKinley are with the Multi-Modality Imaging Laboratory, Departments of Biomedical Engineering and Radiology, Duke University Medical Center, Durham NC 27710 USA.

J. E. Bowsher is with the Department of Radiology, Duke University Medical Center, Durham, NC 27710 USA.

Digital Object Identifier 10.1109/TMI.2005.852501

I. INTRODUCTION

COMPACT, dedicated gamma cameras coupled with a fully three-dimensional (3-D) acquisition system can serve as a secondary diagnostic tool for imaging of breast cancers, particularly in cases when mammographic findings are inconclusive. The significance of a compact camera in single photon emission imaging is its ability to facilitate closer proximity imaging, thus minimizing distance-dependent spatial resolution limitations. An advantage of employing nuclear medicine techniques stems from the fact that the accuracy of scintimammography is unaffected by breast density: studies have shown women with dense breasts may benefit most from this complementary imaging technique [1], [2]. Thus, several groups have investigated compact position-sensitive photomultiplier tube (PSPMT)-based gamma cameras for the breast imaging paradigm [3]–[6].

Compared to planar imaging alone, there is a significant increase in the accuracy of breast imaging for the diagnosis of primary breast cancer when mammography and scintimammography are combined [7]. Diagnostic accuracy may be further improved when using tomography rather than a simple combination of scintimammography and mammography, given that contrast improves with such a 3-D technique. In addition, the 3-D localization of the tumor is provided, as is the potential for *in vivo* quantification of lesion activity. Single photon emission computed tomography (SPECT) specifically for breast imaging has been investigated both with clinical gamma cameras [8]–[17] and dedicated systems [4], [17]–[22]. Our group has previously demonstrated that a compact, fully 3-D hemispherical positioning gantry that allows for imaging with a detector positioned anywhere about a pendant, uncompressed breast phantom significantly improves image quality and lesion visualization [20], [21]. Those studies were performed with quantized NaI(Tl) scintillator, PSPMT-based compact gamma cameras.

While these dedicated PSPMT cameras offer an improvement over clinical gamma cameras, the energy discrimination can be further improved by using cadmium zinc telluride (CZT) semiconductor detectors. The use of CZT detectors for the detection of breast lesions has been previously proposed and investigated through SPECT simulation studies [22] and preprototype measurements [18], and scintimammography measurements [23]. Solid-state detectors made of CZT boast a markedly improved energy resolution over scintillator-based NaI(Tl), with reported measurements of 4%–7% full-width at half-maximum (FWHM)

at 140.6 keV [23]–[27], as compared to NaI(Tl)'s typical energy resolution of 9%–10% [28]. Indeed, for compact gamma cameras utilizing quantized elements, the energy resolution, and hence scatter rejection, is usually poorer still. Scintimammography phantom imaging studies indicate that scatter from cardiac and hepatic background can significantly contaminate the primary lesion signal [29]. While it is generally accepted that better energy resolution performance yields improved emission image quality, it is unclear what specific effect this will have in the 3-D breast imaging paradigm [20], [21].

Using a fully 3-D acquisition geometry discussed here, there is an infinite set of camera trajectories, or orbits, with which to acquire projection data. The camera motions and techniques presented here can also directly be applied to other imaging modalities, such as cone-beam X-ray transmission imaging. The gantry's several degrees of freedom allow any detector, source/detector or even detector/detector connected to it to be positioned anywhere about a 2π steradian solid angle of coverage. For example, by replacing the gamma camera utilized here with a flat-panel digital X-ray detector, combined with an opposing X-ray tube, cone-beam transmission acquisitions of a pendant breast phantom can be performed [30], [31].

While a simple, vertical-axis-of-rotation orbit for an emission imaging camera [13] with a parallel-hole collimator yields a completely sampled volume [32], [33], the imaged breast volume, for example, is smaller than for an acquisition orbit which includes camera tilt. Due to positioning restraints imposed by the detector, the furthest into the breast one can image without tilt is limited to the plane perpendicular to the nipple-chest axis where the camera is adjacent to the torso. Cameras with a large dead edge further decrease the viewable breast volume. One main advantage of fully 3-D orbits that utilize increased polar tilt is an increased viewable breast volume, potentially into the chest wall region [20]. However, with increased tilt angle, the camera may directly view cardiac and hepatic regions that take up the injected radiopharmaceutical, which could contribute primary background contamination to the 2-D projection images of the breast.

Using a compact CZT detector to image lesions in a uniform breast background, the primary aim of this study is to evaluate the imaging ability of the developed emission mammotomography system, both with and without additional torso backgrounds, with some previously investigated and newer trajectories. To our knowledge, this is the first implementation and evaluation of a fully developed CZT detector and system for dedicated tomographic imaging of the breast (mammotomography).

II. PLANAR AND SPECT PERFORMANCE CHARACTERISTICS OF THE CZT DETECTOR

A. Methods

The commercially available, production LumaGEM™ 3200-S camera (Gamma Medica Inc., Northridge, CA) (Fig. 1) utilizes a 60×84 array of $2.5 \times 2.5 \times 6$ mm³ quantized CZT elements. The detector is kept at 15 °C, using water cooling. We evaluated the camera with an unmatched parallel beam, lead collimator with hexagonally arranged holes (1.22-mm hole size flat-to-flat, 0.2-mm septa, 25.4-mm height).

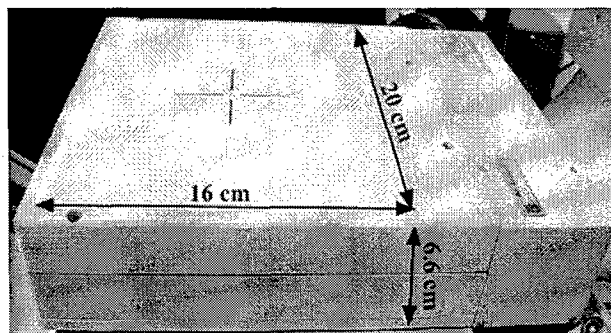


Fig. 1. Photograph of the compact CZT detector with 16×20 cm² field of view (FOV).

With the collimator removed, the intrinsic energy resolution was measured for 10 M total counts using a point source of Tc-99m located approximately 1 m from the camera surface. Count rates were ~ 17.5 kcps using an open energy window (~ 10 kcps in a 16% symmetric ($\pm 8\%$) window about the photopeak). Sensitivity, defined as (counts/sec)/mCi, was measured with a 14-cm-diameter petri dish filled with an ~ 3 -mm layer of 2.6 mCi of Tc-99m, placed 10 cm from the collimator face. Counts were recorded for 60 s. The dose calibrator in our lab has a $\pm 5\%$ error. The sensitivity measurement is based on a 16% symmetric ($\pm 8\%$) energy window about the 140-keV photopeak, which is the window size used for all of the studies performed to characterize the detector (all those found in Section II). Energy windows are applied globally to all pixels, i.e., there is not a separate energy window for each discrete pixel, though in principle there could be.

Planar spatial resolution was measured by acquiring images of a single capillary tube in air, filled with 3.8 mCi of Tc-99m in 6.0 cm of its length. Projection data were acquired with the line source moved across the detector face both horizontally and vertically with respect to the camera, in 1-mm increments for a total of 10 mm. For both the horizontal and vertical directions, the tube was then placed at the position yielding the lowest FWHM, and projection data were acquired at a collimator-to-source distance of 1 through 10 cm. The expected system spatial resolution is a function of the intrinsic and collimator resolutions. Collimator resolution (R_{coll}) was calculated by $R_{\text{coll}} = [d(l_{\text{eff}} + b + c)]/l_{\text{eff}}$, where d is the hole diameter, l_{eff} is the 'effective length' of the collimator holes, b is the distance from the collimator to the radiation source, and c is the collimator-to-detector distance [34], [35]. The effective collimator length is calculated by $l_{\text{eff}} = l - 2\mu^{-1}$, where l is the length of the holes and μ is the linear attenuation coefficient of the collimator material (lead) [34].

Reconstructed spatial resolution was determined from SPECT measurements of two capillary tubes in air, one filled with 3.8 mCi of Tc-99m in 6.0 cm of its length, the other filled with 1.8 mCi of Tc-99m in 3.0 cm, both suspended along the vertical axis of rotation with one placed on the axis of rotation and one offset by 2 cm. Simple circular tomography over 360° was used for these measurements with 128 projections, at 5 s/projection. Acquisitions were made at 3-, 5-, and 7-cm rotation radii. Note that the radius-of-rotation (ROR) is defined as the perpendicular distance from the center of the detector

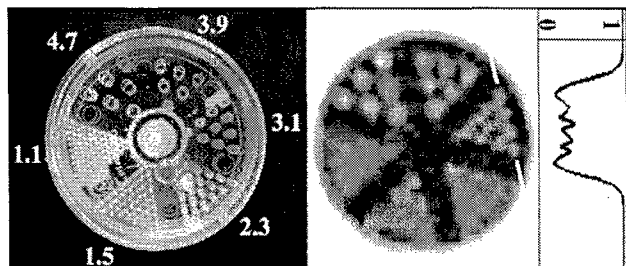


Fig. 2. (Left) Photograph of the mini-rod phantom, with diameters labeled (in mm), with a pitch equal to twice their diameter. (Middle) OSEM reconstructed mini-rod data (8 subsets, 20 iterations, 2.5-mm voxels, 5 summed slices to reduce noise, correction for COR partial pixel shift) acquired with 4.4-cm ROR. (Right) Profile (one-pixel wide) drawn through the 3.1-mm rods at edge, as indicated. Darker grayscale values indicate areas where activity is present (normalized to 1 in this case); white areas (i.e., the rods) are cold.

face, at the front face of the collimator, to the center-of-rotation (COR). Images were reconstructed from projection data using an ordered subsets expectation maximization (OSEM) algorithm [36], [37] implemented with a ray-tracing capability, using 8 subsets, 5 iterations, and 2.5-mm grid voxels. Since spatial resolution was not modeled within these reconstructions, there is a limit to how much spatial resolution the reconstructions can recover, and that limit will be reached within a relatively small number of iterations. The number of subsets was chosen based on previous evaluations of tradeoffs between signal-to-noise ratio (SNR) and contrast of small lesions [20], [21].

A 7.7-cm diameter cylinder containing a resolution-frequency phantom consisting of acrylic mini-rods each 2.6 cm long (model ECT/DLX/MP, Data Spectrum Corp., Hillsborough, NC) was used as another measure of the tomographic spatial resolution of the system (Fig. 2). In each of six sectors, the rods had equal diameters of 4.7, 3.9, 3.1, 2.3, 1.5, and 1.1 mm, spaced on twice their diameter. Water containing 15.6 mCi of Tc-99m filled the interstitial spaces between the rods, thus, images are of "cold" rods. The phantom was oriented such that the rods were vertical, parallel to the axis of rotation. The camera and phantom were both leveled, and the rods were placed in the central portion of the field of view (FOV). The ROR was fixed at 4.4 cm. The 16% energy window yielded count rates of ~ 5.9 kcps. Simple circular tomography was used for these measurements with 256 projections over 360° and an acquisition time of 28 s/projection.

B. Results

Of the detector's 5120 pixels, 99.8% were routinely usable. The dead pixels were randomly dispersed throughout the imaging FOV, with only one bad 4-pixel cluster at the edge of the distal FOV. The system has a dead-pixel correction scheme supplied by the manufacturer, which includes a linear interpolation of the surrounding pixels' values. For our imaging studies, the phantoms did not extend into that portion of the detector. One might expect a similar dead pixel fraction and random distribution from similar imaging devices. Furthermore, extensive quality control studies are performed before each set of experiments; should excessive dead pixels appear to be concentrated in any one region, the modules could be replaced within the camera. The measured uniformity of the

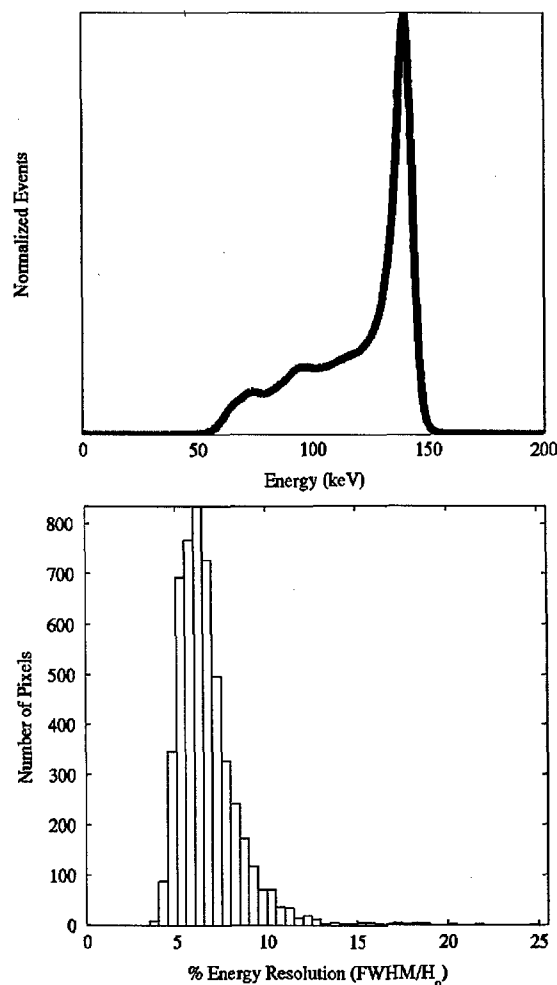


Fig. 3. (Top) Gain balanced, summed energy spectra of all active pixels. As per NEMA-2001 specifications, the measured FWHM energy resolution was 6.8%. (Bottom) Histogram of FWHM Energy Resolutions for all discrete pixels. Mean = 6.7%; Median = 6.4%; Min = 3.5%; Max = 24.8%.

TABLE I
AVERAGE PLANAR SPATIAL RESOLUTION FWHM AND FWTM AS PER [38]

Collimator-Source Distance (cm)	Direction Along Detector			
	Horizontal		Vertical	
	FWHM (mm)	FWTM (mm)	FWHM (mm)	FWTM (mm)
1	3.4 ± 0.7	6.3 ± 0.7	3.7 ± 0.7	6.6 ± 0.4
10	6.7 ± 0.1	12.2 ± 0.3	7.3 ± 0.2	13.0 ± 0.3

detector was $\pm 4.0\%$, given as the overall standard deviation of all pixels divided by the global mean.

The gain balanced, summed energy spectra (Fig. 3) yielded an intrinsic energy resolution of 6.8% FWHM at 140 keV. Using the same protocol for calculation of the FWHM (as per [38]) for each individual pixel resulted in a mean intrinsic energy resolution of 6.7%, with a range of 3.5% to 24.8% (Fig. 3, histogram). The measured sensitivity of the system for the parallel-beam collimator using Tc-99m was 1402 cps/mCi (37.9 cps/MBq).

Average planar spatial resolution FWHM and full-width-tenth-maximum (FWTM) values as measured with the capillary line source, according to [38], for collimator-source distances of 1 and 10 cm are shown in Table I. Planar spatial resolution plotted as a function of distance to the detector compared well

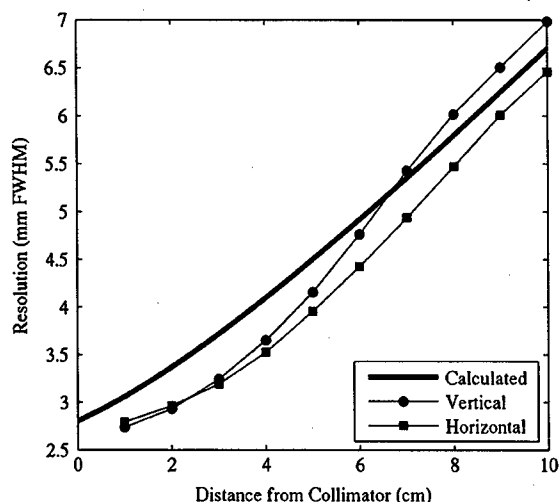


Fig. 4. Planar spatial resolution results from capillary line source measurements match calculated values.

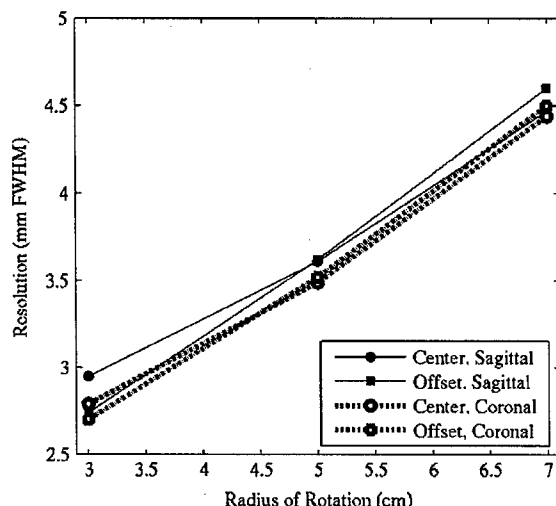


Fig. 5. Reconstructed SPECT spatial resolution results measured through two capillary tubes located at the ROR center and 2-cm offset. Data obtained from 10-pixel-wide profiles drawn in both the coronal and sagittal slices from the fifth iteration of the reconstructed data.

to the calculated system resolution (Fig. 4). Horizontal and vertical measurements may be different due to the line source being ideally aligned with the collimator holes in one case, and/or nonalignment with the Cartesian distribution of the quantized CZT elements. Furthermore, the size and shape of the collimator holes are not matched to the detector elements, and the collimator holes are not aligned with the Cartesian distribution of the square pixels. The system's current unmatched collimator can potentially introduce aliasing and sensitivity fluctuations across an individual detector element. While some groups are investigating un/matched collimator designs for pixellated detectors [39]–[41], it is known that rotating the unmatched collimator with respect to the detector pixels would reduce these effects [42].

SPECT spatial resolution results are shown in Fig. 5 for the fifth iteration data, where 10-pixel-wide profiles were drawn in both the coronal and sagittal slices, and Gaussian curves were fit to the profiles to extract the FWHM information.



Fig. 6. Dedicated emission mammothography system with camera mounted on the hemispherical positioning gantry. A filled anthropomorphic torso phantom and pendant, uncompressed 1060 ml breast are suspended within the camera's FOV.

Resolution measurements are not significantly different with fewer iterations.

Reconstructed results with 8 subsets, 20 iterations, and 2.5-mm voxels, from the mini-rod measurements are shown in Fig. 2. The second sector of rods (3.9-mm diameter) are clearly distinguishable, as would be expected with results from Figs. 4, and 5 given the ROR of 4.4 cm. The 3.1-mm rods are also discernible; though the profile reveals a relatively low contrast, the rods can indeed be resolved.

III. THREE-DIMENSIONAL MAMMOTOMOGRAPHY

The significance of any 3-D orbit with a dedicated breast imaging system is that it allows for fully 3-D imaging of an uncompressed, pendant breast while avoiding physical features or other hindrances from a patient during the acquisition. The tomographic gantry (Fig. 6) used to position the camera's central ray at any point in a hemisphere about the COR has been previously described [20], [21]. A basis set of orbits was initially characterized using a smaller, $12.8 \times 12.8 \text{ cm}^2$ FOV NaI(Tl) camera incorporated onto the dedicated emission mammothograph [21]. While results showed significant improvements in contrasts and SNRs for breast lesions as compared to simple vertical-axis-of-rotation acquisitions and uncompressed planar imaging, the system was limited by the relatively small FOV. Image artifacts resulted from a necessary camera shift to compensate for large, truncated breast volumes.

The new CZT detector used here has a larger FOV and obviates this camera shift of our previous work. Thus, in this work, we evaluate a subset of orbits from [21] here acquired with the full FOV CZT detector. In addition, we evaluate newer orbits. Ideally, an acquisition orbit should: 1) meet Orlov's sampling

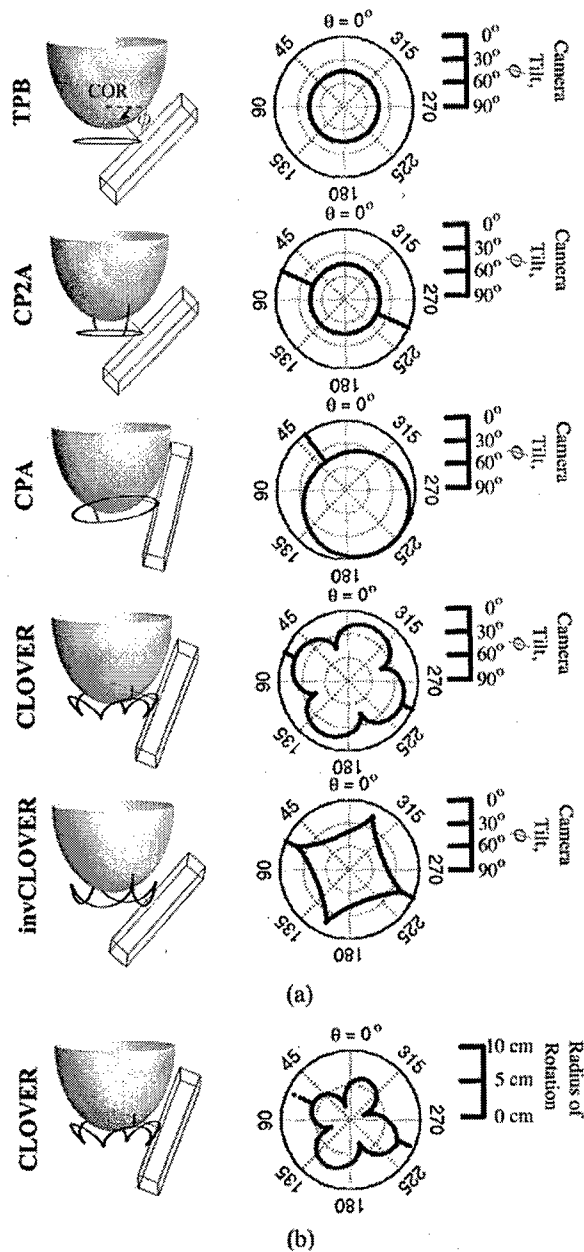


Fig. 7. (a) Scale schematics of orbits, with 1060 ml breast modeled. The wire-frame box represents the $16 \times 20 \text{ cm}^2$ active detector FOV, with center on the trajectory (black orbit path) about the breast. Orbits are (Top to Bottom): Tilted-Parallel-Beam (TPB); Circle-Plus-Two-Arcs (CP2A); Circle-Plus-Arc (CPA); Cloverleaf (CLOVER); and Inverse Cloverleaf (invCLOVER) (see, also, Table III). Labeled in TPB schematic are the: center of rotation (COR), located $\sim 2 \text{ cm}$ inside the breast along the nipple-chest axis; direction of increased polar camera tilt (small arrow). Dark gray line from COR is perpendicular to the detector face. Note that while these implementations meet Orlov's criteria for sufficient sampling, simple modifications allow for more viewable breast volume when physical hindrances preclude sufficient sampling. Next to each 3-D schematic are polar plots of camera polar tilt (ϕ) (plotted as a radius, with 90° at center and 0° at edge) versus azimuthal angle (θ) (plotted around the circle from 0° to 360°). (b) For CLOVER orbit, example polar plot of ROR contouring (0 cm radius at center), which allows camera to move close to the breast, as a function of azimuthal angle (θ).

criterion for sufficient data collection for accurate reconstruction of the activity distribution within the breast when the activity is fully within the camera's FOV for each projection angle [32]; 2) maximize the viewable breast volume; 3) minimize the

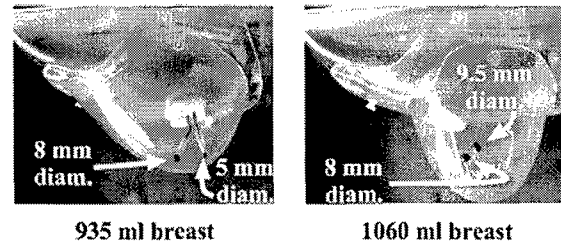


Fig. 8. Photographs of the (left) 935 ml and (right) 1060 ml anthropomorphic breast phantoms. Dimensions of both phantoms are given in Table II. Two sets of embedded lesions were inserted into each phantom as shown.

TABLE II
DIMENSIONS OF THE CUSTOM BREAST PHANTOMS

Breast Volume (ml)	Dimensions (in cm)		
	Superior-Inferior	Nipple-Chest	Medial-Lateral
935	20	7.5	15
1060	16	12	18

background contamination from cardiac and hepatic sources; and 4) contour the breast to minimize the distance related resolution degradations.

If used as a secondary diagnostic tool, the emission mammotomography system evaluated here can image an indeterminate lesion which may have presented on an initial mammogram. Orbits can be designed to contour the breast keeping the detector position near such a lesion. Thus, for this set of experiments, we examine those orbits illustrated in Fig. 7(a). Given the geometry of a pendant breast and the tilts afforded by the system to contour the breast, proximity of different parts of the camera will vary with respect to the breast and an azimuthal axis of rotation. Orbits are designed to optimally contour the breast utilizing dynamic ROR control [example given in Fig. 7(b)], allowing at most a 1-cm separation between the camera's center and the breast phantom surface.

While this paper focuses on parallel-beam imaging utilizing a focal spot at infinity, Orlov's sampling criteria have been shown to be a special case [33] of Tuy's condition for cone-beam sampling [43], which outlines criteria for cone-beam type geometries that are also possible with our system. The flexibility of the gantry allows for investigation of various sampling schemes, for a variety of converging or even diverging collimation beam configurations.

A. Methods

Two acrylic lesions, one 8-mm and one 5-mm inner diameter with $\sim 1\text{-mm}$ wall thickness (Data Spectrum Corp.) were inserted into a $\sim 935 \text{ ml}$ custom fabricated, fillable anthropomorphic breast phantom (Radiology Support Devices Inc., Newport Beach, CA) as shown in Fig. 8. The 8-mm lesion was placed centrally in the breast, while the 5-mm lesion was placed proximally. The custom-made breast phantom is one of several, each with varying sizes and shapes; this particular model has dimensions given in Table II. The dimensions of these phantoms are within the ranges measured clinically [44]. Specific orbit parameters used for these acquisitions, including ROR ranges, are given in Table III. The lesion:breast radionuclide concentration ratio was 9.8:1, with an absolute lesion activity concentration of $12.1 \mu\text{Ci/ml}$. The initial scan was acquired for 20 min, with subsequent acquisitions adjusted to compensate for

TABLE III
ORBIT PARAMETERS USED FOR EACH BREAST PHANTOM ACQUISITION,
WITH ALL ORBITS ACQUIRED OVER A 360° AZIMUTHAL RANGE (θ)

Orbit Name	Acronym	ϕ Range (min-max) (degrees)	ROR Range (min-max) (cm)	Number of Prjs
<i>935 ml Breast, COR located at nipple</i>				
Tilted-Parallel-Beam	TPB	45°	1.9 - 3.7	128
Circle-Plus-Two-Arcs	CP2A	0 - 45°	1.9 - 9.3	162
Circle-Plus-Arc	CPA	0 - 45°	2.4 - 9.3	145
Cloverleaf	CLOVER	0 - 45°	2.0 - 9.3	268
Inverse Cloverleaf	invCLOVER	0 - 45°	2.0 - 9.3	268
<i>1060 ml Breast + Filled Torso, COR located ~2 cm inside nipple</i>				
Tilted-Parallel-Beam	TPB	45°	3.2 - 4.4	128
Circle-Plus-Arc	CPA	15 - 45°	3.8 - 7.1	139
Cloverleaf	CLOVER	15 - 45°	3.6 - 7.2	256
Inverse Cloverleaf	invCLOVER	15 - 45°	3.6 - 7.1	256

TABLE IV
ACTIVITY CONCENTRATION RATIOS FOR EACH OF THE FILLED ORGANS
IN THE ANTHROPOMORPHIC TORSO AND BREAST PHANTOMS

Organ	Volume (ml)	Concentration (μ Ci/ml)	Ratio
Breast	1060	0.33	1.0
Torso	7810	0.33	1.0
Liver	1010	4.2	12.7
Heart (outer wall)	290	4.0	12.1
9.5 mm diam. lesion	0.43	2.0	6.1
8.0 mm diam. lesion	0.26	2.0	6.1

radioactive decay. As in Section II, a $\pm 8\%$ symmetric energy window about the 140-keV photopeak was used, yielding count rates of ~ 0.9 kcps. The breast phantom was attached to the anthropomorphic torso phantom to simulate complications in patient positioning, but the torso was *not* filled with radioactivity.

To more nearly simulate a clinical study and, thus, match the biodistribution of activity in a patient, an anthropomorphic torso phantom containing a heart, liver, and lungs (*Radiology Support Devices Inc.*) was filled according to compiled, published data [3], [4], [45]–[47]. The ~ 1060 ml breast phantom, torso and organs were filled according to the concentration ratios given in Table IV, assuming an initial total dose of 25 mCi (925 MBq), with the heart uptake of 1.2% after 5 min [47]. Two lesions, one 9.5-mm and one 8.0-mm inner diameter with ~ 1 -mm wall thickness (*Data Spectrum Corp.*) were also filled according to the concentration ratios given in Table IV. The 9.5-mm lesion was placed centrally in the breast, while the 8-mm lesion was placed in the upper outer quadrant of the breast (Fig. 8). Total image time was adjusted to compensate for radioactive decay, with the initial scan acquired for 20 min. Because of the expected increase in secondary (scattered) contamination resulting from the filled torso, a tighter energy window was used to reject scatter. Thus, in these breast+filled torso acquisitions, a symmetric $\pm 4\%$ window about the 140-keV photopeak of Tc-99m was used, providing count rates of ~ 0.2 kcps.

For the 3-D camera trajectories implemented in these breast+filled torso experiments, the filled torso distal to the breast introduces background activity which is not uniformly in the FOV for each projection angle. Hence, Orlov's criteria is not strictly met. Thus, the primary design goal for the acquisition orbits shifts from meeting Orlov's criterion to maximizing the viewable breast volume. In order to increase the viewable volume, the COR was located as far inside the breast

as practicable to image near the chest wall. As a result, these orbits have a minimum polar tilt of 15°, with the exception of tilted-parallel-beam (TPB) which maintains a larger, 45° polar tilt (Table III).

Images were again reconstructed from projection data using the OSEM algorithm with ray-tracing capability, with 8 subsets, 5 iterations, calculated attenuation correction assuming a uniform emission volume, and 2.5-mm grid voxels. A 3-D Hann filter with a cutoff of 0.7 times the Nyquist frequency was applied to the reconstructed data.

Regions of interest (ROIs) were drawn both inside the lesions and circumferentially about each lesion in the breast background. For lesion sizes of 9.5-, 8-, and 5-mm-diameter, ROIs contained 12, 9, and 4 pixels, respectively. In all cases, 24 separate background regions were drawn about each lesion, 8 each in the slice containing the lesion's centroid, in the 2.5-mm slice above, and in the 2.5-mm slice below. The size of the background ROIs drawn about each lesion corresponded to the size of the ROI drawn within that lesion (e.g., for the 9.5-mm lesion, 24 background regions totaled 288 pixels, whereas for the 8-mm lesion, 24 background regions totaled 216 pixels).

The SNR was measured as the difference in mean pixel values of the lesion and breast background, divided by the standard deviation of the uniform background ($(ROI_{\text{lesion}} - ROI_{\text{breast}})/\sigma_{\text{breast}}$). Lesion contrast is defined as the signal difference divided by the background signal ($(ROI_{\text{lesion}} - ROI_{\text{breast}})/ROI_{\text{breast}}$).

B. Results

Fig. 9 shows reconstructed results from the 935 ml breast-only measurements, where both lesions are located in the same transaxial plane. Without additional torso contamination, and with a uniform breast background, both the centrally located 8 mm and the proximally located 5-mm-diameter lesions are clearly visible. Table V gives results from calculations of SNR and contrast for both lesions at the second OSEM iteration, smoothed with a Hann filter (which was the optimal tradeoff between gains in contrast and losses in SNR (see [20], [21])).

Fig. 10(a) shows reconstructed results from the 1060 ml breast and filled anthropomorphic torso phantom measurements, for the centrally located 9.5-mm-diameter lesion. Fig. 10(b) shows an example of reconstructed results for the 8-mm lesion. Table V lists results from calculations of SNR and contrast for both the 9.5-mm and 8-mm lesions, again at the second OSEM iteration, smoothed with a Hann filter.

C. Discussion

The two breast phantoms were chosen for these mammotomography studies because of their similar size (volume), but vastly different shape. The breast's shape was purposely and deliberately altered to examine its effect on the newer orbits evaluated within this work. With a different breast shape, various complications in positioning arise (including ROR control to contour the breast) without significantly changing the amount of scatter, total activity, or attenuation that one might expect with vastly different sized breasts.

In studies with the 935 ml breast, high-count, low-noise images result (Fig. 9). This is not surprising given the fairly large energy window ($\pm 8\%$) and large absolute activity. However,

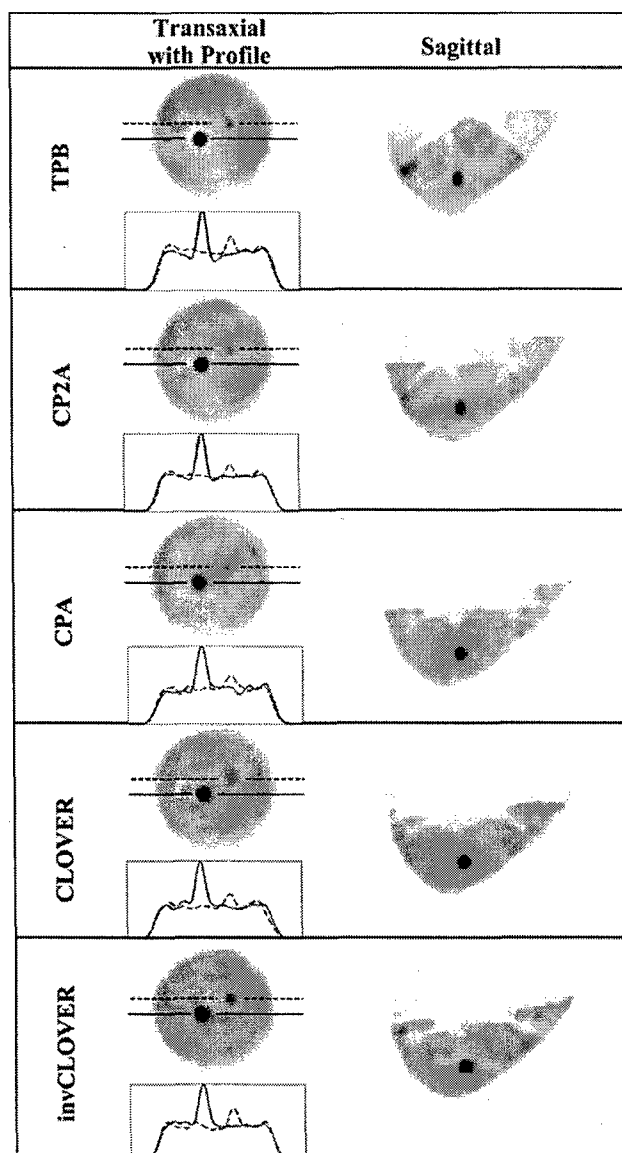


Fig. 9. OSEM reconstructed data (8 subsets, second iteration smoothed with Hann filter shown) from the 935 ml breast data, for each labeled orbit, with a 9.8:1 lesion:breast radionuclide concentration ratio. Solid line in transaxial slice and profile is through the 8-mm lesion, and the dashed line is through the 5-mm lesion. Note that incomplete sampling artifacts from reconstructed data seen with the TPB orbit sagittal views are reduced with the more complex orbits that improve sampling, similar to results shown in [20] and [21].

this ideal case does demonstrate the ability of the system to clearly resolve a 5-mm lesion. Furthermore, both subcentimeter diameter lesions were resolved with each improved 3-D sampling scheme, afforded by the flexibility of the hemispherical positioning gantry, suggesting the viability of these trajectories for clinical studies. With the use of a radio-opaque bed to shield the system from additional body background, we are currently investigating whether the image quality, given enough statistics, could ideally resemble that shown in these isolated breast measurements [48].

The TPB orbit (which does not strictly meet Orlov's sufficiency condition) yields the lowest SNR value for the 5-mm lesion. Further, the reconstructed images are riddled with artifacts, including an elongated nipple-chest axis, similar to our

TABLE V
MEASURED SNRS AND CONTRASTS, AT 2ND OSEM ITERATION,
SMOOTHED WITH A HANN FILTER

Orbit	9.5 mm (0.43 ml)		Lesion Size 8 mm (0.26 ml)		5 mm (0.06 ml)	
	SNR	Contrast	SNR	Contrast	SNR	Contrast
<i>Ideal low-noise case with high uptake:</i>						
<i>935 ml Breast Only</i>						
<i>10:1 activity concentration ratio, 12.1 $\mu\text{Ci/ml}$ in lesions, 16% EWin</i>						
	central		distal			
TPB	—	—	19.3	2.0	2.7	0.2
CP2A	—	—	26.6	1.9	4.9	0.2
CPA	—	—	17.3	1.4	3.9	0.2
CLOVER	—	—	23.2	1.4	7.9	0.3
invCLOVER	—	—	17.1	1.5	6.9	0.3
<i>More realistic case simulating patient biology:</i>						
<i>1060 ml Breast + Filled Torso,</i>						
<i>6.1:1:12 activity concentration ratio, 2.0 $\mu\text{Ci/ml}$ in lesions, 8% EWin</i>						
	central		distal			
TPB	4.6	0.8	3.4	0.5	—	—
CPA	4.8	1.0	5.5	0.6	—	—
CLOVER	3.7	0.8	2.0	0.3	—	—
invCLOVER	6.3	1.2	1.2	0.2	—	—

previous results [20], [21]. With the more complex orbits that improve volumetric sampling, the breast shape is almost fully recovered. Results also indicate that the orbit most optimal for specific lesion locations may change; whether this result is more ascribable to the placement of the lesion or the size of the lesion itself is being further investigated.

The viewable breast volume is limited for the 935 ml breast case along the nipple-chest axis. Because the design criteria included meeting Orlov's sampling criteria, the COR was located at the nipple for this particular breast shape and size. Thus, with the lesions optimally placed near the nipple for this set of measurements, resulting images provided for high contrast resolution. However, for lesions located near the chest wall, relatively far from the detector, a COR located at the nipple may preclude their visualization even given improved sampling. Consequently, design criteria for any orbit require a tradeoff between improved sampling and viewable breast volume.

This subsequent optimization of orbit design parameters was examined in the 1060 ml breast + filled torso experiments. The design goal for the orbit implementations for those measurements was to move the COR as far into the breast as practicable. Accordingly, the minimum tilt was increased from 0° to 15° so that the COR could be moved into the breast ~ 2 cm. This, in turn, increased the viewable breast volume. Indeed, the entire 12-cm length of the nipple-chest wall axis can be seen, as well as some additional depth into the chest wall with only a small missing cone of data behind the chest wall along the nipple-chest axis.

With more realistic uptake ratios in the body and absolute activities of the organs, the 9.5-mm centrally located lesion (~ 6 cm from the nipple) was discernible in all images. Again, results from the TPB orbit in Fig. 10(a) demonstrate the familiar elongation of the nipple-chest axis. Additionally, increased activity from the background, specifically the liver, is also visible [Fig. 10(a), white arrow]. Interestingly, the remaining orbits, though also incompletely sampling the breast according to Orlov's condition, appear to more nearly recover the breast's shape. This suggests that while the mathematical condition for accurate reconstruction of the activity distribution within

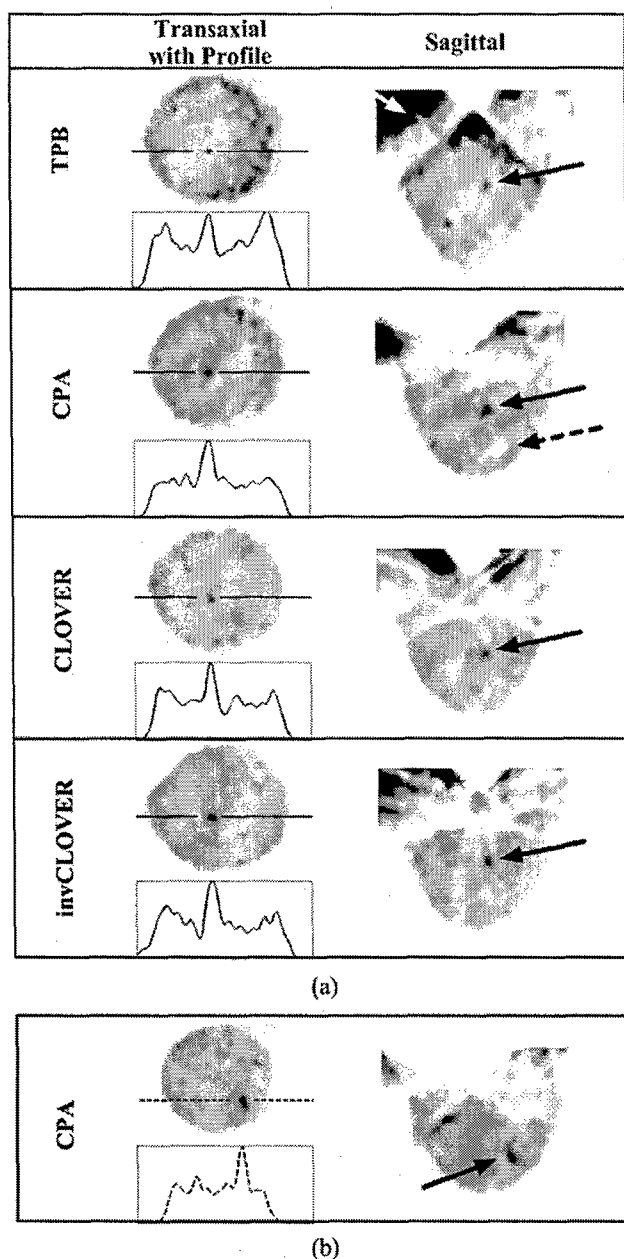


Fig. 10. OSEM reconstructed data (8 subsets, second iteration smoothed with Hann filter shown) from the 1060 ml breast + filled torso data, for each labeled orbit with an incomplete sampling scheme, with a 6.1:1:12 lesion:breast-and-torso:liver-and-heart radionuclide concentration ratio. (a) Solid line is drawn through the 9.5-mm lesion. Note the increased background contamination with TPB (white arrow) as compared to the other orbits which do not maintain the large detector polar tilts, thus limiting more direct views of the heart and liver. Even with these incompletely sampled orbits, and more realistic absolute radioactivities within the phantom, the centrally located 9.5-mm lesion is clearly visible. Dashed arrow in CPA points to cold lesion holder, which can also be seen with the other orbits (see, also, InvCLOVER) and in Fig. 8. (b) Views of the 8-mm lesion at different transaxial and sagittal locations than the larger lesion.

the breast was not met, in practice, the sampling requirement may be less strict than initially anticipated; this is an area that warrants further investigation.

Incomplete sampling may, however, produce false positives in the image [Fig. 10(a), CLOVER]; this may also be due to

other reconstruction artifacts since these misleading signals are actually manifested as streaks and appear in multiple contiguous planes. The more peripheral areas of the breast along the chest wall may suffer from less sufficient sampling; the uniformity of the sampling scheme itself is currently being investigated in addition to completeness issues.

For this work, there was no patient (torso) shielding whatsoever. Given a radio-opaque support bed, however, background activity should be significantly reduced, as the heart and liver should be removed from a significant number of detector vantages. The shielded bed may also affect the allowed camera trajectories. Our group is in the process of implementing and investigating such a patient bed and its effects (and expected improvements) on image quality [48].

IV. CONCLUSION

Dedicated emission mammothography with a CZT imaging detector that could image large breasts was implemented. Initial characterization and preclinical evaluation studies were performed. The intrinsic characteristics of the medium-FOV, semiconductor imaging detector were evaluated, as was the overall suitability of the device for dedicated SPECT imaging of the breast. The detector was found to have a 6.8% FWHM at 140 keV, and was able to clearly discern 3.1-mm-diameter mini-cold rods in reconstructed images. A key benefit provided by a dedicated, compact SPECT breast imaging system is its ability to acquire fully 3-D molecular data about an *uncompressed*, pendant breast and possibly anterior chest wall. As a potential secondary diagnostic tool, the 3-D sampling scheme can be tailored to an individual patient, especially if mammographic studies can provide *a priori* information about a suspected lesion. Though it appears no single orbit optimizes image quality for lesions at all placements within the breast, the phantom studies shown here demonstrate the capability of the system to easily adapt the acquisition scheme for imaging of various breast shapes and sizes. Additionally, there are no outstanding trajectories that consistently yield optimized quantitative lesion imaging parameters. Qualitatively however, while imaging isolated breasts which are completely in the field-of-view for all vantages yields consistent reconstructed images, imaging breasts with realistic torso backgrounds (out-of-field activity) substantially alters image characteristics and breast morphology. Orbits that improve sampling yield more realistic morphology as well as more accurate overall activity distributions throughout the imaged volumes. Furthermore, results from breast phantom measurements reveal the ability of this approach to visualize lesions <1 cm in diameter, and studies are ongoing to evaluate this ability with vastly different sized breast phantoms [48]. The strength of this molecular imaging approach for breast imaging can be further enhanced with additional structural information provided by transmission cone-beam mammothography. Initial development of a prototype X-ray computed mammothograph for such a purpose is underway [30], [31]. The 3-D emission mammothography system evaluated within this work, incorporating a compact CZT detector, shows a promising, clinically relevant technique for molecular imaging of the whole breast.

ACKNOWLEDGMENT

The authors thank K. Parnham, J. Li, and B. E. Patt (*Gamma Medica*) for their assistance with camera operation and modification.

REFERENCES

- [1] I. Khalkhali, J. K. Baum, J. Villaneuva-Meyer, S. L. Edell, L. G. Hanelin, C. E. Lugo, R. Taillefer, L. M. Freeman, C. E. Neal, A. M. Scheff, J. L. Connolly, S. J. Schnitt, M. J. Houlihan, J. S. Sampalis, and S. B. Haber, "99 mTc sestamibi breast imaging for the examination of patients with dense and fatty breasts: Multicenter study," *Radiology*, vol. 222, pp. 149–155, 2002.
- [2] L. R. Coover, G. Caravaglia, and P. Kuhn, "Scintimammography with dedicated breast camera detects and localizes occult carcinoma," *J. Nucl. Med.*, vol. 45, pp. 553–558, 2004.
- [3] M. B. Williams, A. R. Goode, V. Galbis-Reig, S. Majewski, A. G. Weisenberger, and R. Wojcik, "Performance of a PSPMT based detector for scintimammography," *Phys. Med. Biol.*, vol. 45, pp. 781–800, 2000.
- [4] S. Majewski, D. Kieper, E. Curran, C. Keppel, B. Kross, A. Palumbo, V. Popov, A. G. Weisenberger, B. Welch, R. Wojcik, M. B. Williams, A. R. Goode, M. More, and G. Zhang, "Optimization of dedicated scintimammography procedure using detector prototypes and compressible phantoms," *IEEE Trans. Nucl. Sci.*, vol. 48, no. 3, pp. 822–829, Jun. 2001.
- [5] J. Kim, Y. Choi, K. Joo, B. Sihm, J. Chong, S. E. Kim, K. H. Lee, Y. S. Choe, and B. Kim, "Development of a miniature scintillation camera using an NaI(Tl) scintillator and PSPMT for scintimammography," *Phys. Med. Biol.*, vol. 45, pp. 3481–3488, 2000.
- [6] D. P. McElroy, E. J. Hoffman, L. MacDonald, B. E. Patt, J. S. Iwanczyk, Y. Yamaguchi, and C. S. Levin, "Evaluation of breast tumor detectability with two dedicated, compact scintillation cameras," *IEEE Trans. Nucl. Sci.*, vol. 49, no. 3, pp. 794–802, Jun. 2002.
- [7] J. R. Buscombe, J. B. Cwikla, B. Holloway, and A. J. W. Hilson, "Prediction of the usefulness of combined mammography and scintimammography in suspected breast cancer using ROC curves," *J. Nucl. Med.*, vol. 42, pp. 3–8, 2001.
- [8] A. Spanu, G. Dettori, S. Nuvoli, A. Porcu, A. Falchi, P. Cottu, M. E. Solinas, A. M. Scanu, F. Chessa, and G. Madeddu, "99 mTc-Tetrofosmin SPET in the detection of both primary breast cancer and axillary lymph node metastasis," *Eur. J. Nucl. Med.*, vol. 28, pp. 1781–1794, 2001.
- [9] F. H. Fahey, K. L. Grow, R. L. Weber, B. A. Harkness, E. Bayram, and P. H. Hemler, "Emission tuned-aperture computed tomography: A novel approach to scintimammography," *J. Nucl. Med.*, vol. 42, pp. 1121–1127, 2001.
- [10] A. Seret, M. Defrise, and D. Blocklet, "180-degree pinhole SPET with a tilted detector and OS-EM reconstruction: Phantom studies and potential clinical applications," *Eur. J. Nucl. Med.*, vol. 28, pp. 1836–1841, 2001.
- [11] A. Spanu, G. Dettori, P. Chiaramida, P. Cottu, A. Falchi, A. Porcu, M. E. Solinas, S. Nuvoli, and G. Madeddu, "The role of 99 mTc-tetrofosmin pinhole SPECT in breast cancer axillary lymph node staging," *Cancer Biother. Radiopharm.*, vol. 15, pp. 81–91, 2000.
- [12] C. Scarfone, R. J. Jaszcak, J. Li, M. S. Soo, M. F. Smith, K. L. Greer, and R. E. Coleman, "Breast tumor imaging using incomplete orbit pinhole SPET: A phantom study," *Nucl. Med. Commun.*, vol. 18, pp. 18:1077–18:1086, 1997.
- [13] H. Wang, C. Scarfone, K. L. Greer, R. E. Coleman, and R. J. Jaszcak, "Prone breast tumor imaging using vertical axis-of-rotation (VAOR) SPECT systems: An initial study," *IEEE Trans. Nucl. Sci.*, vol. 44, no. 3, pp. 1271–1276, Jun. 1997.
- [14] B. C. Pieper, J. E. Bowsher, M. P. Tornai, J. Peter, and R. J. Jaszcak, "Breast tumor imaging using tiltable head SPECT camera," *IEEE Trans. Nucl. Sci.*, vol. 48, no. 4, pp. 1477–1492, Aug. 2001.
- [15] M. P. Tornai, J. E. Bowsher, R. J. Jaszcak, B. C. Pieper, K. L. Greer, P. H. Hardenbergh, and R. E. Coleman, "Mammotomography with pinhole incomplete circular orbit SPECT," *J. Nucl. Med.*, vol. 44, pp. 585–593, 2003.
- [16] J. E. Bowsher, M. P. Tornai, S. D. Metzler, J. Peter, and R. J. Jaszcak, "SPECT breast imaging using more nearly complete orbits and combined pinhole-parallel-beam collimation," in *IEEE Nucl. Sci. Symp. Conf. Rec.*, vol. 3, Nov. 2001, pp. 1328–1330.
- [17] S. D. Metzler, J. E. Bowsher, M. P. Tornai, B. C. Pieper, J. Peter, and R. J. Jaszcak, "SPECT breast imaging combining horizontal and vertical axes of rotation," *IEEE Trans. Nucl. Sci.*, vol. 49, no. 1, pp. 31–36, Feb. 2002.
- [18] M. P. Tornai, C. N. Archer, J. E. Bowsher, B. E. Patt, J. S. Iwanczyk, L. R. MacDonald, and K. Parnham, "Feasibility of full-field single photon emission mammotomography using a novel CZT detector," in *IEEE Nucl. Sci. Symp. Conf. Rec.*, vol. 3, Nov. 2002, p. 1901.
- [19] R. Pani, A. Soluri, R. Scafe, R. Pellegrini, G. de Vincentis, M. N. Cinti, M. Betti, R. Inches, G. Garibaldi, F. Cusanno, M. Gambaccini, A. Fantini, A. Taibi, A. Olivo, S. Pani, L. Rigon, D. Bollini, N. Lanconelli, and A. Del Guerra, "Feasibility study for SPECT mammography based on compact imagers rotating around breast vertical axis," in *IEEE Nucl. Sci. Symp. Conf. Rec.*, vol. 3, Nov. 2000, pp. 21/36–21/39.
- [20] M. P. Tornai, J. E. Bowsher, C. N. Archer, J. Peter, R. J. Jaszcak, L. R. MacDonald, B. E. Patt, and J. S. Iwanczyk, "A 3-D gantry single photon emission tomograph with hemispherical coverage for dedicated breast imaging," *Nucl. Inst. Meth.*, vol. A497, no. 1, pp. 157–167, 2003.
- [21] C. N. Archer, M. P. Tornai, J. E. Bowsher, S. D. Metzler, B. C. Pieper, and R. J. Jaszcak, "Implementation and initial characterization of acquisition orbits with a dedicated emission mammotomograph," *IEEE Trans. Nucl. Sci.*, vol. 50, no. 3, pp. 418–420, Jun. 2003.
- [22] M. Singh and E. Mumcuoglu, "Design of a CZT based BreastSPECT system," *IEEE Trans. Nucl. Sci.*, vol. 45, no. 3, pp. 1158–1165, Jun. 1998.
- [23] B. Mueller, M. K. O'Connor, I. Blevis, D. J. Rhodes, R. Smith, D. A. Collins, and S. W. Phillips, "Evaluation of a small cadmium zinc telluride detector for scintimammography," *J. Nucl. Med.*, vol. 44, pp. 602–609, 2003.
- [24] J. F. Butler, C. L. Lingren, S. J. Friesenhahn, F. P. Doty, W. L. Ashburn, R. L. Conwell, F. L. Augustine, B. Apotovsky, B. Pi, T. Collins, S. Zhao, and C. Isaacson, "CdZnTe solid-state gamma camera," *IEEE Trans. Nucl. Sci.*, vol. 45, no. 3, pp. 359–363, Jun. 1998.
- [25] Y. Eisen, I. Mardor, A. Shor, Z. Baum, D. Bar, G. Feldman, H. Cohen, E. Issac, R. Haham-Zada, S. Blitz, Y. Cohen, B. Glick, R. Falk, S. Roudeshush, and I. Blevis, "NUCAM3—A gamma camera based on segmented monolithic CdZnTe detectors," *IEEE Trans. Nucl. Sci.*, vol. 49, no. 4, pp. 1728–1732, Aug. 2002.
- [26] G. L. Zeng and D. Gagnon, "CdZnTe strip detector SPECT imaging with a slit collimator," *Phys. Med. Biol.*, vol. 49, pp. 2257–2271, 2004.
- [27] D. G. Marks, H. B. Barber, H. H. Barrett, E. L. Dereniak, J. D. Eskin, K. J. Matherson, J. M. Oolfenden, E. T. Young, F. L. Augustine, W. J. Hamilton, J. E. Venzon, B. A. Apotovsky, and F. P. Doty, "A 48 × 48 CdZnTe array with multiplexer readout," *IEEE Trans. Nucl. Sci.*, vol. 43, no. 3, pp. 1253–1259, Jun. 1996.
- [28] L. Verger, M. C. Gentet, L. Gerfault, R. Guillemaud, C. Mestais, O. Monnet, G. Montemont, G. Petroz, J. P. Rostaing, and J. Rustique, "Performance and perspectives of a CdZnTe-based gamma camera for medical imaging," *IEEE Trans. Nucl. Sci.*, vol. 51, no. 6, pp. 3111–3117, Dec. 2004.
- [29] M. B. Williams, D. Narayanan, M. J. More, P. J. Goodale, S. Majewski, and D. A. Kieper, "Analysis of position-dependent Compton scatter in scintimammography with mild compression," *IEEE Trans. Nucl. Sci.*, vol. 50, no. 5, pp. 1643–1649, Oct. 2003.
- [30] R. L. McKinley, E. Samei, C. N. Brzymialkiewicz, M. P. Tornai, and C. E. Floyd, "Measurements of an optimized beam for x-ray computed mammotomography," in *Proc. SPIE (Phys. Med. Imag.)*, vol. 5368, 2004, pp. 311–319.
- [31] M. P. Tornai, R. L. McKinley, C. N. Brzymialkiewicz, P. Madhav, S. J. Cutler, D. J. Crotty, J. E. Bowsher, E. Samei, and C. E. Floyd, "Design and development of a fully-3D dedicated X-ray computed mammotomographic system," *Proc. SPIE (Physics of Medical Imaging)*, vol. 5745, no. 1, pp. 189–197, 2005.
- [32] S. S. Orlov, "Theory of three dimensional reconstruction," *Sov. Phys. Crystallogr.*, vol. 20, no. 3, pp. 312–314, 1975.
- [33] S. D. Metzler, J. E. Bowsher, and R. J. Jaszcak, "Geometrical similarities of the Orlov and Tuy sampling criteria and a numerical algorithm for assessing sampling completeness," *IEEE Trans. Nucl. Sci.*, vol. 50, no. 5, pp. 1550–1555, Oct. 2003.
- [34] S. R. Cherry, J. A. Sorenson, and M. E. Phelps, *Physics in Nuclear Medicine*, pp. 227–251, 2003.
- [35] H. O. Anger, "Radioisotope cameras," in *Instrumentation in Nuclear Medicine*, G. J. Hine, Ed. New York, NY: Academic, 1967, vol. 1, pp. 485–552.
- [36] H. M. Hudson and R. S. Larkin, "Accelerated image reconstruction using ordered subsets of projection data," *IEEE Trans. Med. Imag.*, vol. 13, no. 4, pp. 601–609, Dec. 1994.
- [37] J. E. Bowsher, D. R. Gilland, C. E. Floyd, R. J. Jaszcak, V. E. Johnson, and R. E. Coleman, "Three dimensional iterative reconstruction for SPECT," *J. Nucl. Med.*, vol. 33, p. 879, 1992, abstract.

- [38] *Performance Measurements of Scintillation Cameras*. NEMA Standards Publication NU 1-2001.
- [39] D. Gunter, K. Matthews II, and C. Ordóñez, "The interaction of collimator lattice periodicity and detector pixelation," in *IEEE Nucl. Sci. Symp. Conf. Rec.*, Nov. 1998, pp. 1525–1531.
- [40] C. Jeanguillaume, A. Douiri, M. Quartuccio, S. Begot, D. Franck, M. Tence, and P. Ballongue, "CACAO a collimation means well suited for pixellated γ -camera," in *IEEE Nucl. Sci. Symp. Conf. Rec.*, Nov. 2001, pp. 2291–2294.
- [41] M. F. Smith, S. Majewski, and A. G. Weisenberger, "Optimizing pin-hole and parallel hole collimation for scintimammography with compact pixellated detectors," *IEEE Trans. Nucl. Sci.*, vol. 50, no. 3, pp. 321–326, Jun. 2003.
- [42] M. A. Kalinosky, D. J. Wagenaar, J. Pawlak, T. Rempel, and J. C. Engdahl, "Aliasing in pixellated detectors," in *Proc. Future Directions in Nuclear Medicine Physics and Engineering*, 1999, p. 41.
- [43] H. K. Tuy, "An inversion formula for cone-beam reconstruction," *SIAM J. Appl. Math.*, vol. 43, pp. 546–552, 1983.
- [44] F. Scopinaro, R. Pani, G. De Vincentis, A. Soluri, R. Pellegrini, and L. Porfiri, "High-resolution scintimammography improves the accuracy of technetium-99m methoxyisobutylisonitrile scintimammography: Use of a new dedicated gamma camera," *Eur. J. Nucl. Med.*, vol. 26, pp. 1279–1288, 1999.
- [45] J. Maublant, M. de Latour, D. Mestas, A. Clemenson, S. Charrier, V. Feillel, G. Le Bouedec, P. Kaufmann, J. Dauplat, and A. Veyre, "Technetium-99m-sestamibi uptake in breast tumor and associated lymph nodes," *J. Nucl. Med.*, vol. 37, no. 6, pp. 922–925, 1996.
- [46] R. Pani, G. De Vincentis, F. Scopinaro, R. Pellegrini, A. Soluri, I. N. Weinberg, A. Pergola, R. Scafe, and G. Trotta, "Dedicated gamma camera for single photon emission mammography (SPEM)," *IEEE Trans. Nucl. Sci.*, vol. 45, no. 6, pp. 3127–3133, Dec. 1998.
- [47] F. J. Th. Wackers, D. S. Berman, J. Maddahi, D. D. Watson, G. A. Beller, H. W. Strauss, C. A. Boucher, M. Picard, B. L. Holman, R. Fridrich, E. Inglese, B. Delaloye, A. Bischof-Delaloye, L. Camin, and K. McKusick, "Technetium-99m hexakis 2-methoxyisobutyl isonitrile: Human biodistribution, dosimetry, safety, and preliminary comparison to thallium-201 for myocardial perfusion imaging," *J. Nucl. Med.*, vol. 30, no. 3, pp. 301–311, 1989.
- [48] C. N. Brzymialkiewicz, M. P. Tornai, R. L. McKinley, and J. E. Bowsher, "3-D data acquisition sampling strategies for dedicated emission mammotomography for various breast sizes," presented at the *2004 IEEE Nucl. Sci. Symp. and Med. Imag. Conf.*, Rome, Italy, Oct. 16–22, 2004.